


Phase-engineered photon correlations in weakly coupled nanofiber cavity QEDZhiming Wu,^{*} Jiahua Li^{✉,†} and Ying Wu[‡]*School of Physics, Huazhong University of Science and Technology, Wuhan 430074, People's Republic of China* (Received 27 November 2023; revised 28 January 2024; accepted 26 February 2024; published 12 March 2024)

A recent experiment [H. S. Han *et al.*, *Phys. Rev. Lett.* **127**, 073604 (2021); see also accompanying online supplemental material] shows that when a three-level V -type atom with two closely lying upper states interacts with the same vacuum radiation field, its excited states enable vacuum-induced coupling (VIC) owing to the quantum interference between the spontaneous emission pathways. Here, we propose a feasible scheme for phase-engineered photon correlations in the presence of the VIC in an optical nanofiber (ONF) cavity quantum electrodynamics (QED) system. Specifically, we show that a phase-dependent strong photon antibunching with high brightness can be generated in the weak-coupling regime of light-atom interactions. This occurs because of the VIC, leading to both the destructive quantum interference between the different pathways for two-photon excitation and the total closed-loop coupling phase. Different types of purely quantum correlations, such as single- and two-photon blockades, can occur by properly tuning the total closed-loop coupling phase adhering on the VIC, and the switch from photon blockade to photon induced tunneling is revealed as well. On the other hand, the strong photon antibunching can be achieved in a broad driving frequency range, which relaxes the requirement for the driving frequency in the ONF cavity QED system. In addition, we compare the analytical and numerical results of the second- and third-order intensity correlation functions, and they are in good agreement. The present study may provide an alternative route to manipulate the few-photon states and have potential applications in single-photon sources and quantum communications.

DOI: [10.1103/PhysRevA.109.033709](https://doi.org/10.1103/PhysRevA.109.033709)**I. INTRODUCTION**

Quantum coherence and interference effects form the foundation of many quantum optical phenomena [1–3]. One method of generating quantum interference is related to relaxation processes such as spontaneous emission, i.e., vacuum-induced coupling (VIC), which is also known as spontaneously generated coherence [4–7]. It is generated by the quantum interference between the spontaneous emission pathways from the excited doublet to a common ground state [8]. The manifestation of the VIC in atomic systems has attracted much attention and given rise to many interesting phenomena, such as resonance fluorescence [9–11], coherent population trapping [12], lasers without inversion [13,14], and so on. So far, the VIC has been investigated theoretically in several systems, including V -type systems [10,15], Λ -type systems [12,16], and ladder-type systems [17] and has been demonstrated experimentally in atomic ensembles [7,16,18–20].

Recently, there has been much interest in various new phenomena originating from quantum interference effect, for example, unconventional photon antibunching caused by destructive quantum interference between the two or more different quantum pathways from a one-photon state transiting to a two-photon state [21,22]. Photon antibunching, also called photon blockade, refers to the fact that the admission of a first photon into the cavity diminishes the probability

for subsequent photons to enter the cavity, which is a purely quantum effect [23,24]. The photon antibunching effect can be useful in achieving single-photon sources device, which is a valuable application in modern quantum optics [25–27]. As compared with conventional photon antibunching induced by the anharmonic energy-level spacing in a quantum optical system with strong nonlinearity, the unconventional photon antibunching caused by the destructive interference can operate in weak nonlinearity, which relaxes the requirements for system nonlinearity [28–31]. Although previous studies of unconventional photon antibunching have mainly focused on employing coherent fields, e.g., laser fields [32,33] and microwave fields [34,35], to generate the destructive interference, employing incoherent processes, i.e., the VIC, to generate the destructive interference in unconventional photon antibunching remains mostly unexplored.

Inspired by previous work [7] that experimentally observed the VIC in a V -type system, here we put forward a phase-engineered unconventional photon antibunching scheme employing the VIC to generate quantum destructive interference. To be specific, the proposed cavity quantum electrodynamics (QED) system consists of a single three-level V -type atom characterized by two closely lying upper states $|1\rangle$ and $|2\rangle$ and one ground state $|0\rangle$ (see Fig. 1 for a sketch). The atom is trapped inside a tapered optical-nanofiber-based (ONF-based) [36–39] single-mode cavity. The two upper states and one ground state form the so-called Δ -type transition and closed-loop coupling via the VIC. Based on experimental realistic atom-cavity parameters, we numerically and analytically calculate the steady-state second- and third-order intensity correlation functions $g^{(2)}(0)$ and $g^{(3)}(0)$ of the cavity field, and

^{*}zhiming@hust.edu.cn[†]Corresponding author: huajia_li@163.com[‡]yingwu2@126.com

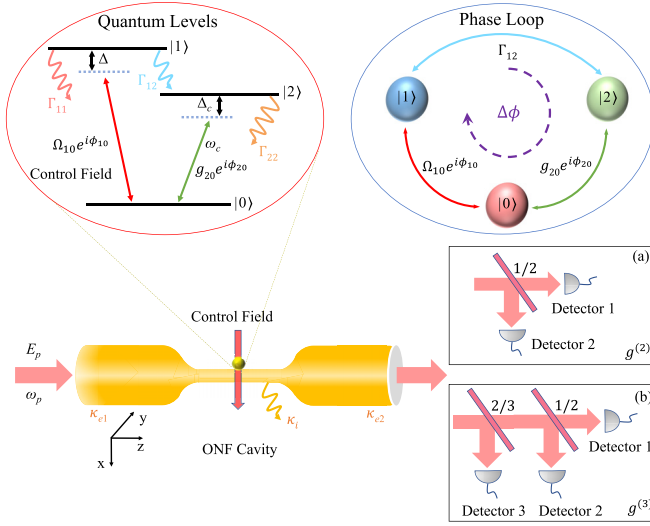


FIG. 1. Schematic illustration of the ONF cavity QED system under consideration. A single three-level V -type atom (the small golden filled circle) is installed in the vicinity of a tapered ONF-based cavity. The atomic level structure, corresponding laser coupling and relevant damping involved in the scheme are shown in the top-left inset. The atomic level structure is composed of a ground state $|0\rangle$ as well as two excited states $|1\rangle$ and $|2\rangle$. The external input probe field with the central frequency ω_p and the amplitude E_p is applied to coherently drive the cavity mode via the left-hand cavity mirror along the axial (z) direction. The cavity mode is coupled to the atomic transition $|2\rangle \leftrightarrow |0\rangle$ with the resonance frequency ω_c and the cavity-atom coupling coefficient $g_{20}e^{i\phi_{20}}$. The free-space control field drives the atomic transition $|1\rangle \leftrightarrow |0\rangle$ with the control-field-atom coupling coefficient $\Omega_{10}e^{i\phi_{10}}$ from the open side of the cavity along the vertical (x) direction. Here Γ_{11} and Γ_{22} represent the damping rates of excited states $|1\rangle$ and $|2\rangle$ to ground state $|0\rangle$, and Γ_{12} denotes the cross-damping rate between the excited states $|1\rangle$ and $|2\rangle$ (i.e., the VIC). The total closed-loop coupling phase $\Delta\phi = \phi_{10} - \phi_{20}$ is shown in the top-right inset, where ϕ_{10} represents the control phase and ϕ_{20} denotes the cavity-atom coupling phase. We can tune $\Delta\phi$ *in situ* by setting, for example, the control phase ϕ_{10} . By employing one ordinary 50 : 50 nonpolarizing beam splitter and two single-photon detectors, the second-order intensity correlation function $g^{(2)}$ of the transmitted field through the right-hand cavity mirror can be measured [see inset (a)]. Similarly, the third-order intensity correlation function $g^{(3)}$ can be measured by using two nonpolarizing beam splitters and three single-photon detectors [see inset (b)]. The total damping rate of the cavity is given by $\kappa = \kappa_{e1} + \kappa_{e2} + \kappa_i$, where κ_{e1} and κ_{e2} represent the damping rates of the left- and right-hand cavity mirrors, and κ_i denotes the inner damping rate of the cavity. The physical meaning of the other symbols used is described in the text.

they are in good agreement. By tuning the total closed-loop coupling phase adhering on the VIC, quantum correlations of photons can be well tuned from antibunching to bunching regimes. We also find that single-photon blockade (1PB), two-photon blockade (2PB), and photon-induced tunneling (PIT) can be achieved by adjusting the total closed-loop coupling phase in a weak-coupling regime of ONF cavity QED. Furthermore, it is possible to obtain the switch from 1PB to 2PB and the switch from 2PB to PIT.

On the other hand, we find that the strong photon antibunching can occur concurrently with high brightness in the

weak-coupling “bad-cavity” regime of cavity QED, offering a guiding significance for practical experimental design to a certain extent and making the experimental realization of our scheme friendly. Moreover, we find that the strong photon antibunching can be achieved in a broad parameter region of driving detuning, which can relax the requirement for the driving frequency in the ONF cavity QED system. We also explore the experimental feasibility of the proposed scheme with existing state-of-the-art ONF cavity QED architecture. By tuning the total closed-loop coupling phase adhering on the VIC, the statistical properties of the cavity field can be easily controlled, which may be useful for the construction of single-photon sources and may have potential applications in quantum information processing [40,41] and quantum communications [42,43].

Such an ONF cavity QED system has been studied previously [44]. However, differently from our previous work [44], our present scheme introduces an additional degree of freedom in the ONF cavity QED system with VIC, namely, an *in situ* tunable phase, due to the closed-loop coupling configuration (see inset of Fig. 1). We focus on the influence of this phase on photon correlation. We find that the introduced closed-loop phase plays an important role in modifying the photon statistical properties of the system. By tuning the phase appropriately, the photon statistics properties of the system can be engineered and the switching between bunching and antibunching can be realized. This indicates that these phase-dependent results offer a more flexible control method to tune and engineer photon statistics, where we can achieve selective photon antibunching. Besides this, the phase-sensitive higher-order (like third-order) intensity correlation behaviors are also explored.

The paper is organized as follows: Section II details the theoretical model and the Hamiltonian of the ONF cavity QED system. Section III discusses the experimental feasibility of our proposed scheme and introduces the choice of typical ONF cavity QED system parameters in detail. Section IV provides the closed-form solutions for the second-order intensity correlation function in the limit of weak driving. Section V presents the in-depth results of the photon statistics for the cavity field. Finally, the paper is summarized in Sec. VI. In Appendix A, we compare the second-order intensity correlation function versus the total closed-loop coupling phase with the VIC and without the VIC. In Appendixes B and C, we provide a detailed derivation for the closed-form solutions for the phase-dependent second- and third-order intensity correlation functions in the limit of weak driving. In Appendix D, we present an analysis of the slight discrepancy between the analytical and numerical results.

II. PHYSICAL SYSTEM AND THEORETICAL FRAMEWORK

As depicted schematically in Fig. 1, the investigated ONF cavity QED system consists of a single three-level V -type atom (the small gold sphere) with one ground state $|0\rangle$ as well as two excited states $|1\rangle$ and $|2\rangle$ trapped in a tapered ONF-based cavity, which is similar to that adopted in Ref. [44]. The damping rate Γ_{ij} of atomic levels induced by the second-order coupling between $|i\rangle$ and $|j\rangle$ ($i, j = 1, 2$) can be expressed as

$\Gamma_{ij} = \vec{d}_{i0} \cdot \vec{d}_{j0} \omega_{i0}^3 / (3\pi \epsilon_0 \hbar c^3)$ [7], where i and j represent the atomic levels. Here, \vec{d}_{i0} and ω_{i0} denote the transition electric-dipole moment and the excited resonance frequency between $|i\rangle$ and $|0\rangle$ (the same applies to \vec{d}_{j0}), ϵ_0 stands for the permittivity of vacuum, \hbar represents the reduced Planck constant, and c is the speed of light. The VIC on $|1\rangle \leftrightarrow |2\rangle$ is subject to dephasing at the rate Γ_{12} , where Γ_{12} denotes the cross-damping rate between the excited states $|1\rangle$ and $|2\rangle$ [7]. Meanwhile, Γ_{11} and Γ_{22} represent the damping rates of the excited states $|1\rangle$ and $|2\rangle$ to the ground state $|0\rangle$, respectively. Assuming that all the transition dipole moments are parallel to each other and real, we can obtain $\Gamma_{12} \simeq \sqrt{\Gamma_{11}\Gamma_{22}}$ like Refs. [7,19,45]. The atomic transition $|2\rangle \leftrightarrow |0\rangle$ is coupled to the cavity mode with frequency detuning $\Delta_c = \omega_{20} - \omega_c$ (ω_{20} is the excited resonance frequency of the atomic transition $|2\rangle \leftrightarrow |0\rangle$ and ω_c is the resonance frequency of the cavity mode) and the cavity-atom coupling coefficient $g_{20}e^{i\phi_{20}}$, where g_{20} represents the cavity-atom coupling strength and ϕ_{20} denotes the cavity-atom coupling phase. The cavity mode is driven by an external laser field with the central frequency ω_p and the amplitude E_p via the left-hand cavity mirror along the horizontal axial direction (axis z). The frequency detuning of the driving laser from the cavity mode is $\Delta_p = \omega_c - \omega_p$. In addition, the free-space control field $\vec{E}_{10}(t) = \vec{e}\mathcal{E}_{10}e^{-i\omega t + i\vec{k}\cdot\vec{r} + i\phi_{10}}$ is used to drive the atomic transition $|1\rangle \leftrightarrow |0\rangle$ with frequency detuning $\Delta = \omega_{10} - \omega$ (ω_{10} is the excited resonance frequency of the atomic transition $|1\rangle \leftrightarrow |0\rangle$ and ω is the central frequency of the control field) in the vertical direction (axis x), where \vec{e} is the unit polarization vector of the control field and denotes its polarization direction, \mathcal{E}_{10} is the amplitude of the control field, $\vec{k} \cdot \vec{r}$ denotes the spatial distribution of the control field and can be ignored in the electric-dipole approximation, and ϕ_{10} represents the control phase (i.e., the initial phase of the control field). The atomic transitions $|0\rangle \xrightarrow{\Omega_{10}e^{i\phi_{10}}} |1\rangle \xrightarrow{\Gamma_{12}} |2\rangle \xrightarrow{g_{20}e^{i\phi_{20}}} |0\rangle$ form a closed-loop configuration (see the top-right inset of Fig. 1), in which Ω_{10} represents the control-field Rabi frequency. The various coupling phases are linked to each other through the closed-loop configuration, leading to the total closed-loop coupling phase $\Delta\phi = \phi_{10} - \phi_{20}$ playing a crucial role, as will be elaborated below.

Based on the above description, the total Hamiltonian of the ONF cavity QED system with the rotating-wave and electric-dipole approximations can be expressed as (assuming the Hamiltonian will be taken to have units of frequency here and hereafter)

$$\hat{H}_{\text{tot}} = \omega_c \hat{a}^\dagger \hat{a} + \omega_{10} \hat{\sigma}_{11} + \omega_{20} \hat{\sigma}_{22} + (g_{20} e^{i\phi_{20}} \hat{a} \hat{\sigma}_{02}^\dagger + \Omega_{10} e^{-i\omega t + i\phi_{10}} \hat{\sigma}_{01}^\dagger + i\eta e^{-i\omega_p t} \hat{a}^\dagger + \text{H.c.}), \quad (1)$$

where $\hat{\sigma}_{lm} = |l\rangle\langle m|$ ($l, m = 0, 1, 2$) denotes the raising ($l > m$), lowering ($l < m$), or population ($l = m$) operator for the atom, with $\hat{\sigma}_{lm}^\dagger = |m\rangle\langle l| = \hat{\sigma}_{ml}$; \hat{a} and \hat{a}^\dagger are the photon annihilation and creation operators of the internal cavity mode, satisfying the bosonic commutation relations $[\hat{a}, \hat{a}^\dagger] = 1$, $[\hat{a}^\dagger, \hat{a}^\dagger] = 0$, and $[\hat{a}, \hat{a}] = 0$. Above, the symbol H.c. stands for the Hermitian conjugate. The parameter g_{20} is the cavity-atom coupling strength (ϕ_{20} is the cavity-atom coupling phase) for the atomic transition $|2\rangle \leftrightarrow |0\rangle$, yielded by $g_{20} = d_{20} \sqrt{\omega_c / (2\hbar \epsilon_0 V)}$, where d_{20} represents the electric-dipole

moment of the corresponding transition $|2\rangle \leftrightarrow |0\rangle$ and V denotes the mode volume of the ONF cavity. The parameter Ω_{10} is the control-field Rabi frequency (ϕ_{10} is the control phase) for the atomic transition $|1\rangle \leftrightarrow |0\rangle$, obtained from $\Omega_{10} = d_{10} \mathcal{E}_{10} / (2\hbar)$ (our definition of the control-field Rabi frequency Ω_{10} corresponds to half of the standard definition of the Rabi frequency), where d_{10} represents the electric-dipole moment of the corresponding transition $|1\rangle \leftrightarrow |0\rangle$ and \mathcal{E}_{10} denotes the amplitude of the control field. Finally, the parameter η is the strength of the external driving laser to populate the cavity mode \hat{a} , expressed as $\eta = \sqrt{\kappa_{e1}} E_p = \sqrt{P_p \kappa_{e1} / (\hbar \omega_p)}$, where P_p represents the pump power of the external driving laser [46,47].

By applying a unitary transformation to a rotating coordinate frame described by the unitary operator $\hat{U}(t) = \exp(-i\hat{H}_0 t)$, where $\hat{H}_0 = \omega_p \hat{a}^\dagger \hat{a} + \omega \hat{\sigma}_{11} + \omega_p \hat{\sigma}_{22}$, and utilizing the relationship $\hat{H}_{\text{rot}} = \hat{U}^\dagger(t) \hat{H}_{\text{tot}} \hat{U}(t) - i\hat{U}^\dagger(t) \partial \hat{U}(t) / \partial t$ [48], eventually we can rewrite the total Hamiltonian (1) as

$$\hat{H}_{\text{rot}} = \Delta_p \hat{a}^\dagger \hat{a} + \Delta \hat{\sigma}_{11} + (\Delta_p + \Delta_c) \hat{\sigma}_{22} + (g_{20} e^{i\phi_{20}} \hat{a} \hat{\sigma}_{02}^\dagger + \Omega_{10} e^{i\phi_{10}} \hat{\sigma}_{01}^\dagger + i\eta \hat{a}^\dagger + \text{H.c.}), \quad (2)$$

where the detunings are defined as $\Delta_p = \omega_c - \omega_p$ (referred to as the driving detuning), $\Delta = \omega_{10} - \omega$ (referred to as the control detuning), and $\Delta_c = \omega_{20} - \omega_c$ (referred to as the cavity detuning).

Without loss of generality, we can set the transformation $\hat{\sigma}_{01} \rightarrow \hat{\sigma}_{01} e^{i\phi_{10}}$ and $\hat{\sigma}_{02} \rightarrow \hat{\sigma}_{02} e^{i\phi_{20}}$, which leads to the total closed-loop coupling phase $\Delta\phi = \phi_{10} - \phi_{20}$ playing a crucial role in engineering quantum correlation behaviors of the system. Based on this transformation and taking the incoherent (dissipative) processes into consideration, the complete dynamics of the ONF cavity QED system with the joint atom-cavity density-matrix operator $\hat{\rho}$ is described by the Lindblad master equation in the Born-Markov approximation [7,48–51]:

$$\begin{aligned} \frac{\partial \hat{\rho}}{\partial t} = & -i[\hat{H}_{\text{tra}}, \hat{\rho}] + \kappa \mathcal{D}(\hat{a})\hat{\rho} + \Gamma_{11} \mathcal{D}(\hat{\sigma}_{01})\hat{\rho} + \Gamma_{22} \mathcal{D}(\hat{\sigma}_{02})\hat{\rho} \\ & + \Gamma_{12} e^{i\Delta\phi} (\hat{\sigma}_{01} \hat{\rho} \hat{\sigma}_{02}^\dagger - \hat{\sigma}_{02}^\dagger \hat{\sigma}_{01} \hat{\rho} / 2 - \hat{\rho} \hat{\sigma}_{02}^\dagger \hat{\sigma}_{01} / 2) \\ & + \Gamma_{12} e^{-i\Delta\phi} (\hat{\sigma}_{02} \hat{\rho} \hat{\sigma}_{01}^\dagger - \hat{\sigma}_{01}^\dagger \hat{\sigma}_{02} \hat{\rho} / 2 - \hat{\rho} \hat{\sigma}_{01}^\dagger \hat{\sigma}_{02} / 2), \quad (3) \end{aligned}$$

with

$$\hat{H}_{\text{tra}} = \Delta_p \hat{a}^\dagger \hat{a} + \Delta \hat{\sigma}_{11} + (\Delta_p + \Delta_c) \hat{\sigma}_{22} + (g_{20} \hat{a} \hat{\sigma}_{02}^\dagger + \Omega_{10} \hat{\sigma}_{01}^\dagger + i\eta \hat{a}^\dagger + \text{H.c.}), \quad (4)$$

where κ represents the total damping rate of the ONF cavity (i.e., $\kappa = \kappa_{e1} + \kappa_{e2} + \kappa_i$), Γ_{11} and Γ_{22} denote the damping rates of excited states $|1\rangle$ and $|2\rangle$ to ground state $|0\rangle$, Γ_{12} stands for the VIC, and the brackets $[\cdot, \cdot]$ indicate the commutator. The above Lindblad superoperator $\mathcal{D}(\hat{O})$ describes the dissipative coupling to the environment and is given by the form $\mathcal{D}(\hat{O})\hat{\rho} = \hat{O}\hat{\rho}\hat{O}^\dagger - \hat{O}^\dagger\hat{O}\hat{\rho}/2 - \hat{\rho}\hat{O}^\dagger\hat{O}/2$ for the collapse operator \hat{O} corresponding to the specific dissipation process. More specifically, the first term on the right-hand side (RHS) of Eq. (3) generates a coherent unitary evolution of the whole system. The second term denotes the decoherence effect of the environment on the system with the total damping rate κ of the ONF cavity and generates the corresponding incoherent

dynamics of the system. The third and fourth terms on the RHS of Eq. (3) correspond to the dissipation of the excited states $|1\rangle$ and $|2\rangle$ into the environment with the damping rates Γ_{11} and Γ_{22} , respectively. Finally, the last two terms on the RHS of Eq. (3) stand for the VIC effect resulting from the dissipative coupling between the excited states $|1\rangle$ and $|2\rangle$ into the environment with the cross-damping rate Γ_{12} [7].

Here, the dynamics of the full atom-ONF-cavity composite system is modeled by the Lindblad master equation [see Eq. (3)]. Note that, both the external “huge”¹ vacuum environment and the ONF-cavity environment simultaneously affect the atomic spontaneous emission rate. In deriving Eq. (3), according to the standard method [48–52], we have taken the trace over the external huge vacuum environment, which accounts for the atomic spontaneous emission and the ONF-cavity photon loss and which corresponds to the Lindblad superoperator parts [see the second to sixth terms on the right-hand side of Eq. (3)] describing the dissipation of the system. However, we do not further trace out the degrees of freedom of the ONF-cavity mode to only study the atomic subsystem, due to its “small” ONF-cavity environment in the considered system. That is to say, the Lindblad master equation (3) has included the obvious influence of the ONF-cavity mode on the atomic spontaneous emission rate. In this sense, the ONF-cavity subsystem belongs to the internal component of the whole system under study. On the other hand, when we take the trace over the ONF-cavity mode under certain conditions (if the ONF-cavity mode is regarded as an external environment like the vacuum mode), indeed the atomic spontaneous emission rate is significantly modified and correspondingly the form of the Lindblad master equation (3) is also changed where an effective spontaneous emission rate can be obtained [52]. This effective spontaneous emission rate of the isolated atom is composed of two parts: (i) the emission rate of the atom to its original vacuum environment and (ii) the emission rate of the atom through the ONF-cavity mode into the cavity environment. The ratio of the latter to the former is called the Purcell factor [53]. Nevertheless, the above handling method after taking the trace over the ONF-cavity environment is not necessary for the problem we are studying, because it actually complicates the problem. So, under the form of Eq. (3) given here, the atomic spontaneous emission rate resulting from the vacuum environment is kept unchanged.

There are a few remarks in order here. The various coupling phases are interconnected through the closed-loop configuration $|0\rangle \xleftrightarrow{\Omega_{10}e^{i\phi_{10}}} |1\rangle \xleftrightarrow{\Gamma_{12}} |2\rangle \xleftrightarrow{g_{20}e^{i\phi_{20}}} |0\rangle$ (see the top-right inset of Fig. 1), resulting in the total closed-loop coupling phase $\Delta\phi$ adhering on the VIC (i.e., Γ_{12}). In any observables resulting from Eq. (3), the total closed-loop coupling phase $\Delta\phi$ adhering on the VIC is important.

Alternatively, it can be clearly seen from the atomic level structure of the top-left inset in Fig. 1 that two possible pathways from state $|0\rangle$ to state $|2\rangle$ exist: the direct one $|0\rangle \xleftrightarrow{g_{20}e^{i\phi_{20}}} |2\rangle$ and the indirect one $|0\rangle \xleftrightarrow{\Omega_{10}e^{i\phi_{10}}} |1\rangle \xleftrightarrow{\Gamma_{12}} |2\rangle$. The role of the total closed-loop coupling phase $\Delta\phi$ on the quantum

correlation behaviors in the closed-loop three-level system can be explained from quantum interference induced by these two pathways. From Eqs. (3) and (4), one can see that only the total closed-loop coupling phase $\Delta\phi$ is important and no individual phase-dependent terms appear. In addition, in the cases of the total closed-loop coupling phase $\Delta\phi$ adhering on the cavity-atom coupling strength g_{20} and the control-field Rabi frequency Ω_{10} , there are still no individual phase-dependent terms appearing. We also verify the equivalence for the total closed-loop coupling phase adhering on three different positions (not shown here). It is worth emphasizing that the phase dependence would vanish provided that either of the cavity-atom coupling strength g_{20} , the control-field Rabi frequency Ω_{10} , and the VIC (i.e., Γ_{12}) is switched off (see Appendix A).

In the present work, we primarily focus on the statistical properties of the transmitted photons from the cavity mode \hat{a} in this ONF cavity QED system (see Fig. 1). In general, for a time-independent Hamiltonian (4), the system will tend toward a steady state as $t \rightarrow \infty$ corresponding to $\partial\hat{\rho}/\partial t = 0$. In this circumstance, the statistical properties of the transmitted field can be expediently characterized by the normalized delayed second- and third-order intensity correlation functions [54,55]

$$g^{(2)}(\tau_1) = \frac{\langle \hat{a}^\dagger \hat{a}^\dagger(\tau_1) \hat{a}(\tau_1) \hat{a} \rangle}{\langle \hat{a}^\dagger \hat{a} \rangle^2}, \quad (5)$$

$$g^{(3)}(\tau_1, \tau_2) = \frac{\langle \hat{a}^\dagger \hat{a}^\dagger(\tau_1) \hat{a}^\dagger(\tau_1 + \tau_2) \hat{a}(\tau_1 + \tau_2) \hat{a}(\tau_1) \hat{a} \rangle}{\langle \hat{a}^\dagger \hat{a} \rangle^3}, \quad (6)$$

where the symbol $\langle \cdot \rangle$ represents the quantum expectation value. Here τ_1 represents the delay time between the arrival of the first and second photons and τ_2 denotes the delay time between the arrival of the second and third photons. When the system reaches its steady state $\hat{\rho}_{ss}$ (i.e., $\partial\hat{\rho}_{ss}/\partial t = 0$), the normalized equal-time (or zero-time-delay) second- and third-order intensity correlation functions can be written as

$$g^{(2)}(0) = \frac{\langle \hat{a}^\dagger \hat{a}^\dagger \hat{a} \hat{a} \rangle}{\langle \hat{a}^\dagger \hat{a} \rangle^2} = \frac{\text{Tr}(\hat{\rho}_{ss} \hat{a}^\dagger \hat{a}^\dagger \hat{a} \hat{a})}{[\text{Tr}(\hat{\rho}_{ss} \hat{a}^\dagger \hat{a})]^2}, \quad (7)$$

$$g^{(3)}(0) = \frac{\langle \hat{a}^\dagger \hat{a}^\dagger \hat{a}^\dagger \hat{a} \hat{a} \hat{a} \rangle}{\langle \hat{a}^\dagger \hat{a} \rangle^3} = \frac{\text{Tr}(\hat{\rho}_{ss} \hat{a}^\dagger \hat{a}^\dagger \hat{a}^\dagger \hat{a} \hat{a} \hat{a})}{[\text{Tr}(\hat{\rho}_{ss} \hat{a}^\dagger \hat{a})]^3}, \quad (8)$$

where Tr represents the trace and the normalized equal-time third-order intensity correlation function $g^{(3)}(0, 0)$ can be simply expressed as $g^{(3)}(0)$.

For any classical states, the second-order equal-time correlation function satisfies $g^{(2)}(0) > 1$, which corresponds to super-Poissonian photon-number statistics often called photon bunching. The states for which $g^{(2)}(0) < 1$ correspond to the sub-Poissonian photon-number statistics, which is a non-classical effect often called photon antibunching [44,56,57]. The above-mentioned condition is also used to identify the presence of 1PB [i.e., $g^{(2)}(0) \rightarrow 0$], where two photons (or multiple photons) never occupy the cavity at the same time. In general, the single-photon component in a sub-Poissonian light source dominates over the multiphoton states. Specially, the value of $g^{(2)}(0) = 1$ is referred to as the coherent-state photon corresponding to the Poissonian photon-number statistics. For 2PB, the criterion must be met with $g^{(2)}(0) > 1$ and $g^{(3)}(0) < 1$, which implies two-photon bunching and

¹“Huge” indicates that the environment contains a sufficiently large number of modes.

three-photon antibunching [33,58]. Similar to PIT (i.e., photon bunching) describes a phenomenon that the admission of a first photon into the cavity increases the probability for subsequent photons to enter the cavity, which can be measured by the conditions of $g^{(2)}(0) > 1$ and $g^{(3)}(0) > 1$.

In what follows, we can calculate the normalized equal-time second- and third-order intensity correlation functions $g^{(2)}(0)$ and $g^{(3)}(0)$ of the system by numerically solving the master equation (3) within a truncated Hilbert space under the steady state. In the weak-driving regime, we take the truncated photon number $N = 10$ to obtain the numerical results, while in the strong-driving regime, we take the truncated photon number $N = 20$ for the numerical simulations. The truncated photon numbers for the weak and strong driving regimes are sufficient to guarantee the convergence of the numerical simulations, which will be demonstrated in Appendix D. Alternatively, we can also calculate the normalized equal-time second- and third-order intensity correlation functions $g^{(2)}(0)$ and $g^{(3)}(0)$ of the system by analytically solving the Schrödinger equation (B2) in two-photon excitation and three-photon excitation in Appendixes B and C. The detailed quantum correlation results are presented in Figs. 2–10 below in various parameter spaces.

III. EXPERIMENTAL FEASIBILITY AND TYPICAL PARAMETERS FOR THE MODEL

To illustrate this ONF cavity QED strategy, we propose below a possible implementation. On the one hand, as an example, ^{85}Rb atom (nuclear spin $I = 5/2$, D_2 line, and wavelength 780 nm) on the $5^2S_{1/2} \rightarrow 5^2P_{3/2}$ transition provides an ideal candidate for the three-level dipole emitter [7,59]. The state $|5^2S_{1/2}, F = 3\rangle$ is chosen as the ground state $|0\rangle$; the states $|5^2P_{3/2}, F = 4\rangle$ and $|5^2P_{3/2}, F = 3\rangle$ correspond to the two excited states $|1\rangle$ and $|2\rangle$ (see Fig. 1), respectively. Here F represents the total angular-momentum quantum number, which marks the hyperfine state. The damping rate of the excited state $|1\rangle$ to the ground state $|0\rangle$ is $\Gamma_{11} = 2\pi \times 6.1$ MHz, whereas the damping rate of the excited state $|2\rangle$ to the ground state $|0\rangle$ is $\Gamma_{22} = 5/9 \times 2\pi \times 6.1$ MHz because the excited state $|2\rangle$ decays to the ground state $|0\rangle$ only fractionally with the branching ratio of $5/9$ [7,59,60]. Assuming that all the transition dipole moments are parallel to each other and real, the cross-damping rate between the excited states $|1\rangle$ and $|2\rangle$ is $\Gamma_{12} \simeq \sqrt{\Gamma_{11}\Gamma_{22}} = \sqrt{5/9} \times 2\pi \times 6.1$ MHz (i.e., the VIC) [7].

On the other hand, a tapered ONF-based cavity provides an ideal fiber-in-line platform for the experimental implementation of the ONF cavity QED system [39]. Technique for the fabrication of the tapered ONF is to heat a commercial single-mode optical fiber to soften the silica sufficiently that it can be pulled and tapered [38]. The ONF-based cavity can be produced by introducing two photonic crystal (PC) defect structures into the ONF using a femtosecond laser ablation method [61,62], referred to as the PC nanofiber cavity. Alternatively, the ONF-based cavity can be formed by laser-writing two fiber Bragg gratings (FBGs) into the ONF (i.e., by drilling periodic nanogrooves on the ONF) using a focused ion beam milling method [63,64], referred to as the FBG nanofiber cavity. A combination of PC and FBG structures in the nanofiber

cavity, referred to as the PC-FBG nanofiber cavity, has also been reported in Ref. [65].

Furthermore, as shown in Refs. [37,39,66–72], trapping a single atom in the vicinity of the ONF can be achieved through currently available technologies. For example, following the approach introduced in Refs. [37,66,70], a two-color optical dipole trap can be designed through applying a red- and blue-detuned evanescent light field around the ONF. First, the atoms from a background rubidium vapor are loaded into a standard six-beam magneto-optical trap (MOT). Followed by sub-Doppler cooling, single atoms are loaded into the two-color optical dipole trap using an optical molasses stage. After loading single cold atoms into this nanofiber trap, the MOT beams are shut off and a waiting time is set to ensure that only single atoms trapped here are excited or probed with light launched into the nanofiber. For a detailed description of such atom cooling and atom trapping in the neighborhood of the ONF, see Refs. [37,66,70]. Alternatively, adopting the method described in Refs. [39,71,72], an atom can be cooled and trapped in the lattice of an optical tweezer, which is coupled to an ONF cavity.

Finally, it is pointed out that we consider a specific situation where the cavity is a nanofiber with a pair of built-in FBGs. In such a cavity, the cavity field is a guided field strongly confined in the transverse direction, with a small effective cross-sectional area [61]. Consequently, even in scenarios where the ONF-based cavity exhibits a relatively low cavity finesse and long cavity length, it is still possible to achieve significant atom-field coupling [37,73]. The motivation for employing the nanofiber cavity is to generate the guided-mode photon antibunching in a controllable way, enabling a long-distance transmission for quantum communication purposes. For instance, the damping rates for the left- and right-hand cavity mirrors are equal, with the values $\kappa_{e1} = \kappa_{e2} = 2\pi \times 1.6$ MHz. The inner damping rate of the ONF cavity mode is $\kappa_i = 2\pi \times 3.2$ MHz. The total damping rate of the ONF cavity mode is $\kappa = 2\pi \times 6.4$ MHz. For the cavity length $L = 33$ cm [37], its finesse (roughly the number of intracavity photon round trips during the cavity decay time) is $F = \pi c / (\kappa L) = 71$ with c being the speed of light. We select the typical cavity-atom coupling strength $g = 2\pi \times (2.9, 7.8)$ MHz within a reasonable range of experimental parameters [37,73–75].

Without loss of generality, we can set the cavity-atom coupling phase to zero (i.e., $\phi_{20} = 0$), so that the total closed-loop coupling phase $\Delta\phi = \phi_{10} - \phi_{20} = \phi_{10}$ is dominated by the control phase ϕ_{10} . Before interacting with the atom, the control field can be individually controlled through an electro-optic modulator (EOM) and the control phase can be tuned by phase locking between the GHz microwave generator and the EOM [76,77]. Alternatively, the control phase can be tuned by an arbitrary waveform generator with an in-phase and quadrature mixer [78].

IV. ANALYTICAL INSIGHTS INTO THE PHASE-DEPENDENT SECOND- AND THIRD-ORDER INTENSITY CORRELATION FUNCTIONS

Before proceeding with our numerical calculations, we study analytical solutions and compare them with the

numerical results to better understand the influence of the VIC and the total closed-loop coupling phase on the second- and third-order intensity correlation functions. In the following, we describe our solutions to the probability amplitude coefficients C_{jn} [j represents the three-level atom in the state of $|j\rangle$ ($j = 0, 1, 2$) and n denotes the photon number ($n = 0, 1, 2$) for the Fock state of the cavity mode] for the equations of motion for our ONF cavity QED system in the limit of weak

driving. We then derive the closed-form expressions for the second-order (see Appendix B) and third-order (see Appendix C) intensity correlation functions.

With this purpose, the probability amplitude coefficients $C_{01}[\Delta\phi]$ and $C_{02}[\Delta\phi]$ ($[\Delta\phi]$ represents that C_{01} and C_{02} are functions related to $\Delta\phi$) for the second-order intensity correlation function, whose determination is detailed in Appendix B, can be explicitly given by

$$C_{01}[\Delta\phi] = \frac{ie^{i\Delta\phi}[2e^{i\Delta\phi}g_{20}\Omega_{10}\Gamma_{12}(4X_{01} + \Delta'_p\Gamma_{12}^2) + \eta(-16\Delta'_cY_{01} + 4Z_{01}\Gamma_{12}^2 - \Delta'_p\Gamma_{12}^4)]}{2g_{20}\eta\Omega_{10}\Gamma_{12}(A - \Gamma_{12}^2) + e^{i\Delta\phi}(16\Delta'B + 4C\Gamma_{12}^2 + \Delta'_p\Gamma_{12}^4)}, \quad (9)$$

$$C_{02}[\Delta\phi] = \frac{-4e^{3i\Delta\phi}g_{20}^2\Omega_{10}^2\Gamma_{12}^2 - 4e^{2i\Delta\phi}g_{20}\eta\Omega_{10}\Gamma_{12}(2X_{02} - \Gamma_{12}^2) - e^{i\Delta\phi}\eta^2(16Y_{02} + 4Z_{02}\Gamma_{12}^2 + \Gamma_{12}^4)}{\sqrt{2}[2g_{20}\eta\Omega_{10}\Gamma_{12}(A - \Gamma_{12}^2) + e^{i\Delta\phi}(16\Delta'B + 4C\Gamma_{12}^2 + \Delta'_p\Gamma_{12}^4)]}, \quad (10)$$

where

$$\begin{aligned} A &= 4g_{20}^2 - 4(\Delta'_p + \Delta')(\Delta'_p + \Delta'_c), \\ B &= [g_{20}^2 - \Delta'_p(\Delta'_p + \Delta'_c)][\Omega_{10}^2\Delta'_c + (\Delta'_p + \Delta') \\ &\quad \times (g_{20}^2 - \Delta'_p\Delta'_c)], \\ C &= \Delta'_p\Delta'(-2g_{20}^2 + 2\Delta'_p\Delta'_c + \Delta'_p{}^2) \\ &\quad - (\Omega_{10} - \Delta'_p)(\Omega_{10} + \Delta'_p)[-g_{20}^2 + \Delta'_p(\Delta'_p + \Delta'_c)], \\ X_{01} &= (\Delta'_p + \Delta')[-g_{20}^2 + \Delta'_p(\Delta'_p + \Delta'_c)], \\ Y_{01} &= [\Omega_{10}^2 + \Delta'(\Delta'_p + \Delta')][-g_{20}^2 + \Delta'_p(\Delta'_p + \Delta'_c)], \\ Z_{01} &= \Delta'_p[g_{20}^2 + \Omega_{10}^2 - \Delta'_p(\Delta'_p + \Delta'_c)] \\ &\quad + \Delta' [g_{20}^2 - \Delta'_p(\Delta'_p + 2\Delta'_c)], \\ X_{02} &= g_{20}^2 + \Omega_{10}^2 - 2(\Delta'_p + \Delta')(\Delta'_p + \Delta'_c), \\ Y_{02} &= [\Omega_{10}^2 + \Delta'(\Delta'_p + \Delta')][g_{20}^2 + \Delta'_c(\Delta'_p + \Delta'_c)], \\ Z_{02} &= -g_{20}^2 - \Omega_{10}^2 + \Delta'_p(\Delta'_p + \Delta'_c) + \Delta'(\Delta'_p + 2\Delta'_c), \end{aligned} \quad (11)$$

with $\Delta'_p = \Delta_p - i\kappa/2$, $\Delta' = \Delta - i\Gamma_{11}/2$, and $\Delta'_c = \Delta_p + \Delta_c - i\Gamma_{22}/2$.

Based on the solutions for the probability amplitude coefficients $C_{01}[\Delta\phi]$ [Eq. (9)] and $C_{02}[\Delta\phi]$ [Eq. (10)], the normalized equal-time second-order intensity correlation function $g^{(2)}(0)[\Delta\phi]$ can be further expressed as

$$g^{(2)}(0)[\Delta\phi] \simeq \frac{2|C_{02}[\Delta\phi]|^2}{|C_{01}[\Delta\phi]|^4}. \quad (12)$$

According to Eqs. (9)–(12), the detailed analytical expression of the second-order intensity correlation function $g^{(2)}(0)[\Delta\phi]$ can be obtained. However, the analytical expression of the second-order intensity correlation function $g^{(2)}(0)[\Delta\phi]$ is rather cumbersome and, for the sake of brevity, is not presented here. Nevertheless, it is obvious that the statistical property of photons is closely related to the VIC (i.e., Γ_{12}) and the total closed-loop coupling phase $\Delta\phi$ [cf. Eqs. (9) and (10)]. From the $g^{(2)}(0)[\Delta\phi]$ expression in Eqs. (9)–(12), we predict that the statistical property of photons is modified due to the introduction of the VIC and the total closed-loop

coupling phase since it appears in the probability amplitude coefficients $C_{01}[\Delta\phi]$ [Eq. (9)] and $C_{02}[\Delta\phi]$ [Eq. (10)]. Also, we would like to point out that the closed-form solution and its steady-state behavior under weak driving scenarios are in good agreement with the direct numerical solution of the master equation, which will be verified in the next section.

The probability amplitude coefficients for the third-order intensity correlation function are not shown here. For more details see Appendix C. The analytical solution of the third-order intensity correlation function and its steady-state behavior under weak driving scenarios are in good agreement with the direct numerical solution of the master equation, which will also be verified in the next section.

V. RESULTS AND DISCUSSIONS ABOUT PHASE-SENSITIVE QUANTUM CORRELATIONS $g^{(2)}(0)$ AND $g^{(3)}(0)$

In this section, we focus on the influence of the total closed-loop coupling phase $\Delta\phi$ adhering on the VIC for the ONF cavity QED system. First of all, we present the normalized equal-time second- and third-order intensity correlation functions $g^{(2)}(0)$ (the red-dotted lines) and $g^{(3)}(0)$ (the blue-solid lines) as a function of the driving detuning $\Delta_p/2\pi$ in Figs. 2(a)–2(d), corresponding to the four different total closed-loop coupling phases $\Delta\phi = \{0, \pi/2, \pi, 3\pi/2\}$. The phenomenon of strong photon antibunching corresponds to single-photon emission, often referred to as 1PB. Meanwhile, the photon antibunching requires the suppression of the higher-order correlations, such as $g^{(3)}(0)$. The deep dips of $g^{(3)}(0)$ (the blue-solid lines) in Figs. 2(a)–2(d) demonstrate that the photon antibunching operates beyond second-order processes and suppresses multiphoton events. For example, when $\Delta\phi = 0$ and $\Delta_p/2\pi = 0$ [see Fig. 2(a)], a strong antibunching [$g^{(2)}(0) \simeq 0.05$] can be observed, at which point it exhibits a single-photon purity $P = 1 - g^{(2)}(0) = 0.95$ in the ONF cavity QED system [79,80]. The blue area in Figs. 2(b) and 2(d) indicate the photon bunching [i.e., $g^{(2)}(0) > 1$], which is also called PIT. It is obvious from Figs. 2(a)–2(d) that the photon antibunching and photon bunching (the blue area) can be achieved by appropriately adjusting the total closed-loop coupling phase $\Delta\phi$.

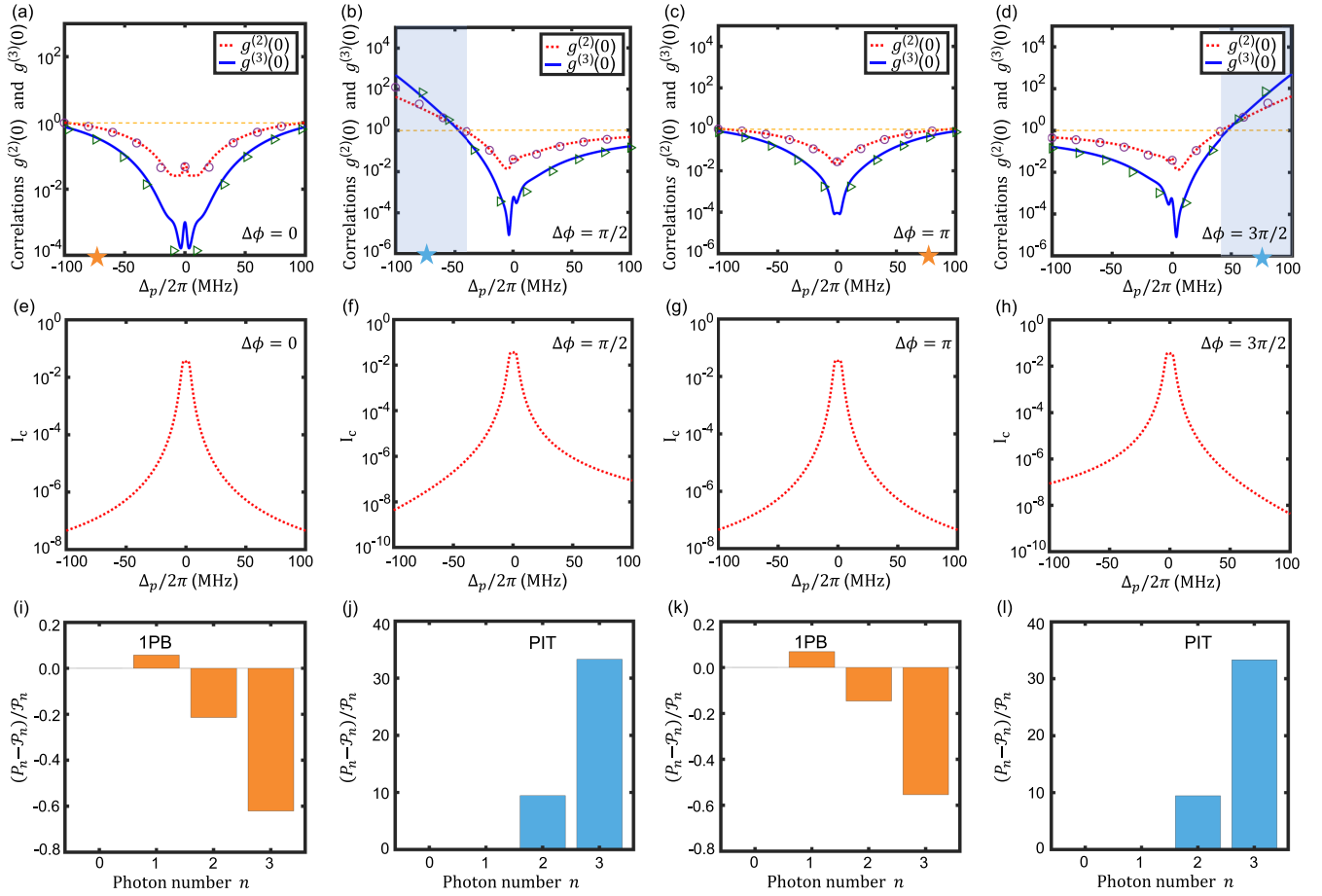


FIG. 2. (a)–(d) The normalized equal-time second- and third-order intensity correlation functions $g^{(2)}(0)$ (the red-dotted lines) and $g^{(3)}(0)$ (the blue-solid lines) as a function of the driving detuning $\Delta_p/2\pi$, corresponding to the four different total closed-loop coupling phases $\Delta\phi = \{0, \pi/2, \pi, 3\pi/2\}$. The red-dotted lines and the blue-solid lines are the numerical results calculated directly by the quantum master equation (3). The purple circles are the analytical results of $g^{(2)}(0)$ calculated by the closed-form expressions (9)–(12) and the green triangles are the analytical results of $g^{(3)}(0)$ calculated by the closed-form expression (C11) (see Appendix C). The blue area in panels (b) and (d) indicate the photon bunching, which is also called photon-induced tunneling (PIT). (e)–(h) The intensity I_c of the ONF-based cavity emission light as a function of the driving detuning $\Delta_p/2\pi$ corresponding to panels (a)–(d), respectively. (i)–(l) The deviations of the photon distribution P_n from the standard Poisson distribution \mathcal{P}_n with the photon number n corresponding to the pentagram markers in panels (a)–(d), respectively. Panels (i) and (k) show single-photon blockade (1PB) (orange bars), while the panels (j) and (l) show PIT (blue bars). The system parameters for all panels are $\kappa/2\pi = 6.4$ MHz, $\Gamma_{11}/2\pi = 6.1$ MHz, $\Gamma_{22}/2\pi = 5/9 \times 6.1$ MHz, $\Gamma_{12}/2\pi = \sqrt{5/9} \times 6.1$ MHz, $g_{20}/2\pi = 2.9$ MHz, $\Omega_{10}/2\pi = 0.65$ MHz, $\eta/2\pi = 0.01$ MHz, $\Delta/2\pi = 0$ MHz, and $\Delta_c/2\pi = 0$ MHz, which are typical values from a recent experiment [7].

The statistical properties of photon antibunching and photon bunching can be more intuitively illustrated by comparing the photon distribution P_n with the standard Poisson distribution \mathcal{P}_n . Here, P_n represents the probability of finding n photons in the ONF-based cavity emission light by $P_n = \sum_j |C_{jn}|^2 / N$ [j represents the three-level atom in the state of $|j\rangle$ ($j = 0, 1, 2$), n denotes the photon number ($n = 0, 1, 2, 3$) for the Fock state of the cavity mode, and $N = \sum_{jn} |C_{jn}|^2$ indicates the normalized constant] [81] and the determination of C_{jn} is detailed in Appendix C. In the limit of weak driving, the normalized constant can be reasonably omitted because $N \simeq 1$. \mathcal{P}_n is the standard Poisson distribution, expressed as $\mathcal{P}_n = \langle \hat{a}^\dagger \hat{a} \rangle^n \exp(-\langle \hat{a}^\dagger \hat{a} \rangle) / n!$ [81–83]. The deviations of the photon distribution P_n from the standard Poisson distribution \mathcal{P}_n with the photon number n are shown

in Figs. 2(i)–2(l), corresponding to the pentagram markers in Figs. 2(a)–2(d), respectively. The pentagram markers in Figs. 2(a)–2(d) correspond to the driving detunings $\Delta_p/2\pi = \{-75, -75, 75, 75\}$ MHz, respectively. The pentagram markers in Figs. 2(b) and 2(d) are located in the blue area. As shown in Figs. 2(i) and 2(k), it can be observed that $P_1 > \mathcal{P}_1$, $P_2 < \mathcal{P}_2$, and $P_3 < \mathcal{P}_3$, which is a clear signature of 1PB corresponding to the photon antibunching at the pentagram markers in Figs. 2(a) and 2(c). Furthermore, in Figs. 2(j) and 2(l), we can find that $P_2 > \mathcal{P}_2$ and $P_3 > \mathcal{P}_3$, which represents PIT corresponding to the photon bunching at the pentagram markers in Figs. 2(b) and 2(d). By tuning the total closed-loop coupling phase $\Delta\phi$, quantum correlations of photons can be well tuned from antibunching to bunching regimes.

To compare the analytical solutions of equal-time second- and third-order intensity correlation functions $g^{(2)}(0)$ and $g^{(3)}(0)$ derived by the Schrödinger equation (see Appendixes B and C) in the steady state with the numerical solutions given by the master equation (3), we also present the fitting results as shown in Figs. 2(a)–2(d). In Figs. 2(a)–2(d), the red-dotted lines and the blue-solid lines represent the numerical results, while the purple circles and the green triangles denote the analytical results. It is revealed that the full numerical solutions obtained by the master-equation approach can be well reproduced by the analytical solutions obtained by the Schrödinger equation approach in the steady state under weak-driving condition. The slight discrepancy between the analytical solutions and the full numerical solutions is discussed in Appendix D below.

In addition, following the standard input-output formalism from quantum optics [84,85], we can achieve the transmission amplitude \hat{S}_{out} of the system, with the form $\hat{S}_{\text{out}} = \sqrt{\kappa_{e2}}\hat{a}$ (κ_{e2} is the damping rate of the right-hand cavity mirror). We also plot the intensity $I_c = \langle \hat{S}_{\text{out}}^\dagger \hat{S}_{\text{out}} \rangle = \kappa_{e2} \langle \hat{a}^\dagger \hat{a} \rangle$ (collected photons per second, i.e., the so-called source brightness [86]) of the ONF-based cavity emission light varying with the driving detuning $\Delta_p/2\pi$ in Figs. 2(e)–2(h), corresponding to the four different cases of Figs. 2(a)–2(d), respectively. By looking at Figs. 2(a)–2(h), we find the strong antibunching effect occurring concurrently with high brightness in the ONF cavity QED system. This implies that the ONF cavity QED system can be regarded as an effective single-photon source device, offering a guiding significance for practical experimental design to a certain extent.

In light of the above analysis, we can see that the total closed-loop coupling phase $\Delta\phi$ has an important influence on the photon statistics of the ONF cavity QED system. To more clearly show the influence of the total closed-loop coupling phase $\Delta\phi$, we plot the normalized equal-time second- and third-order intensity correlation functions $g^{(2)}(0)$ (the red-dotted lines) and $g^{(3)}(0)$ (the blue-solid lines) as a function of the total closed-loop coupling phase $\Delta\phi/\pi$ in Figs. 3(a) and 3(b), corresponding to the two different cases of $\Delta_p/2\pi = -36$ MHz [see Fig. 3(a)] and $\Delta_p/2\pi = -12$ MHz [see Fig. 3(b)]. The purple circles and the green triangles correspond to the analytical results, which are in good agreement with the numerical results (the red-dotted lines and the blue-solid lines). In the scenario of the nonresonant case, we explore the existence of 2PB, which can be judged by the criterion $g^{(2)}(0) > 1$ and $g^{(3)}(0) < 1$. By tuning the total closed-loop coupling phase $\Delta\phi/\pi$, 2PB can occur (the pink area) and the photon statistics of the ONF cavity QED system can be well tuned among 1PB-2PB-PIT regimes [see Fig. 3(a)]. Furthermore, by adjusting the driving frequency [i.e., $\Delta_p/2\pi = -12$ MHz; see Fig. 3(b)], we can see that the 2PB effect can be enhanced and the region where 2PB occurs can be increased. Our results can be further confirmed by comparing the photon distribution P_n with the standard Poisson distribution \mathcal{P}_n . Figures 3(c) and 3(d) show that $P_2 > \mathcal{P}_2$ and $P_3 < \mathcal{P}_3$, which represents 2PB corresponding to the pentagram markers at $\Delta\phi/\pi = 0.65$ in the pink area of Figs. 3(a) and 3(b). Moreover, it can be seen from Figs. 3(c) and 3(d) that the 2PB effect is enhanced by adjusting the driving frequency [see Fig. 3(d)], which is consistent with that shown

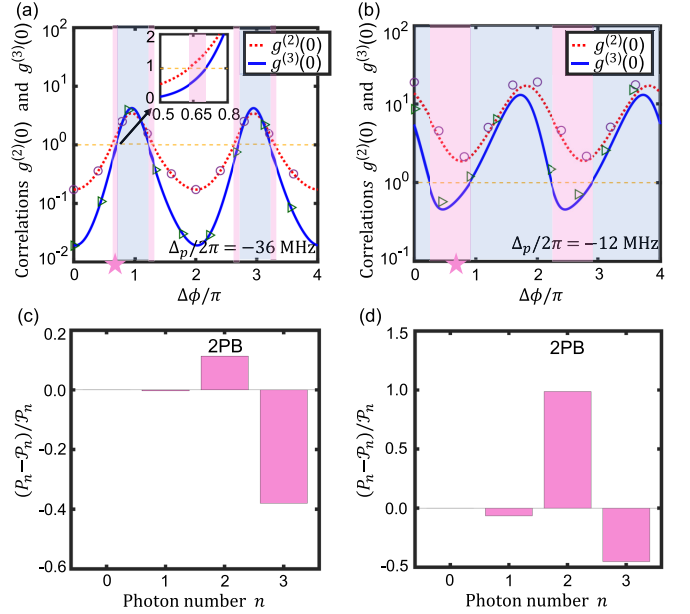


FIG. 3. (a), (b) The normalized equal-time second- and third-order intensity correlation functions $g^{(2)}(0)$ (the red-dotted lines) and $g^{(3)}(0)$ (the blue-solid lines) as a function of the total closed-loop coupling phase $\Delta\phi/\pi$, corresponding to the driving detuning (a) $\Delta_p/2\pi = -36$ MHz and (b) $\Delta_p/2\pi = -12$ MHz. The red-dotted lines and the blue-solid lines correspond to the numerical results, while the purple circles and the green triangles correspond to the analytical results. The pink areas in panels (a) and (b) indicate the occurrence of two-photon blockade (2PB), i.e., $g^{(2)}(0) > 1$ and $g^{(3)}(0) < 1$. The blue areas in panels (a) and (b) indicate the photon bunching. The inset in panel (a) shows an enlarged view of the first pink area, where the inset uses the normal vertical axis to better display the enlarged result. (c), (d) The deviations of the photon distribution P_n from the standard Poisson distribution \mathcal{P}_n with the photon number n corresponding to the pentagram markers in panels (a) and (b), respectively. Panels (c) and (d) show 2PB (pink bars). The other parameters are $\kappa/2\pi = 6.4$ MHz, $\Gamma_{11}/2\pi = 6.1$ MHz, $\Gamma_{22}/2\pi = 5/9 \times 6.1$ MHz, $\Gamma_{12}/2\pi = \sqrt{5}/9 \times 6.1$ MHz, $g_{20}/2\pi = 2.9$ MHz, $\Omega_{10}/2\pi = 0.65$ MHz, $\eta/2\pi = 0.01$ MHz, $\Delta/2\pi = 10$ MHz, and $\Delta_c/2\pi = 20$ MHz.

in Figs. 3(a) and 3(b). Physically, the photon antibunching is due to the quantum interference effect in the three-level Δ configuration induced by the VIC. According to the above coupling and drivings, we display the schematic diagram of the energy levels and excitation pathways of the coupled ONF cavity QED system corresponding to the three-photon manifold, as shown in Fig. 4. From this figure, it is worth emphasizing that the quantum interference can occur between the different excitation pathways thanks to the introduction of the VIC for the closed-loop transition structure. For example, for two-photon excitation, there exist two different excitation pathways to the two-photon excitation state $|0, 2\rangle$. Pathway (i) is the direct pathway, where two photons are directly excited to the two-photon excitation state from $|0, 0\rangle \xrightarrow{\eta} |0, 1\rangle \xrightarrow{\sqrt{2}\eta} |0, 2\rangle$ via the external driving. Pathway (ii) is the indirect pathway facilitated by the control field and the VIC, from which the photons are excited to the two-photon excitation state through $|0, 0\rangle \xrightarrow{\Omega_{10}} |1, 0\rangle \xrightarrow{\eta} |1, 1\rangle \xrightarrow{\Gamma_{12}e^{i\Delta\phi}/2} |2, 1\rangle \xrightarrow{\sqrt{2}g_{20}}$

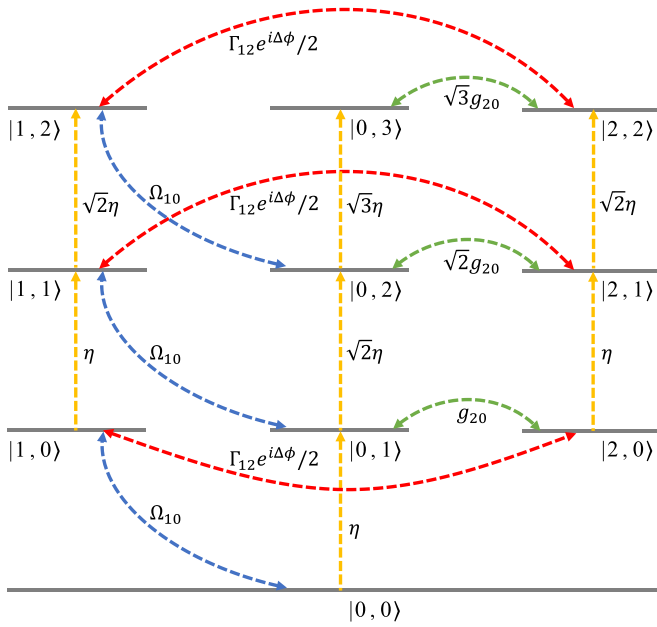


FIG. 4. Schematic diagram of the energy levels and excitation pathways of the coupled ONF cavity QED system corresponding to Fock states up to three photons. Energy-level diagram shows the zero-, one-, two-, and three-photon states (horizontal gray lines without arrows) and the transition pathways (color lines with arrows) leading to the quantum interference in charge of the strong photon antibunching. States are labeled by $|j, n\rangle$ with the first number being the three-level atom in the state of $|j\rangle$ ($j = 0, 1, 2$) and the second number representing the Fock state for the cavity mode with the photon number $n = 0, 1, 2, 3$. The yellow double arrows indicate the different energy-level transitions as a result of the coupling of the external driving laser with the strength η . The green double arrows denote the different energy-level transitions caused by the cavity-atom coupling g_{20} . The blue double arrows mean the different energy-level transitions resulting from the control-field Rabi frequency Ω_{10} . The red double arrows represent the different energy-level transitions induced by the total closed-loop coupling phase $\Delta\phi$ adhering on the VIC (i.e., $\Gamma_{12}e^{i\Delta\phi}$). The destructive quantum interference between the different transition pathways leads to unconventional photon antibunching. By tuning the total closed-loop coupling phase $\Delta\phi$ adhering on the VIC, quantum correlations of photons can be well tuned.

$|0, 2\rangle$. The destructive interference of different excitation pathways (i) and (ii) makes the probability of two-photon excitation state $|0, 2\rangle$ considerably decreasing. As a result, no photons can occupy the state $|0, 2\rangle$, leading to the strong antibunching effect (i.e., 1PB) in the ONF cavity QED system. Similarly, for the other parameters, due to the quantum interference between different excitation pathways, the photons cannot occupy the three-photon excitation state $|0, 3\rangle$, while the probability of two-photon excitation state $|0, 2\rangle$ is nonzero, resulting in the existence of 2PB in the ONF cavity QED system. As can be seen from Fig. 4, the total closed-loop coupling phase $\Delta\phi$ adhering on the VIC (the red double arrows) can affect the quantum interference between different excitation pathways (detailed in Appendix A), thus the photon statistics of the ONF cavity QED system can be well tuned by adjusting the total closed-loop coupling phase $\Delta\phi$. On

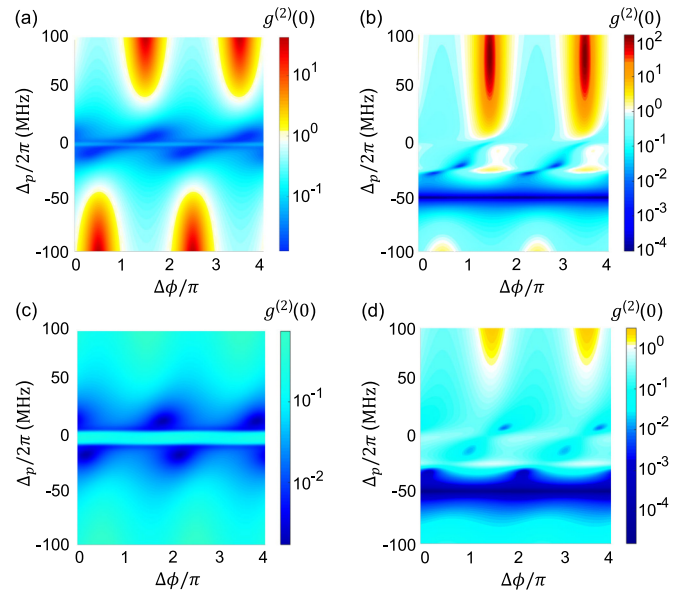


FIG. 5. (a), (b) Contour plot of the normalized equal-time second-order intensity correlation function $g^{(2)}(0)$ as a function of the total closed-loop coupling phase $\Delta\phi/\pi$ as well as the driving detuning $\Delta_p/2\pi$ with $g_{20}/2\pi = 2.9$ MHz, corresponding to the cavity detuning (a) $\Delta_c/2\pi = 0$ and (b) $\Delta_c/2\pi = 50$ MHz. (c), (d) Contour plot of the normalized equal-time second-order intensity correlation function $g^{(2)}(0)$ as a function of the total closed-loop coupling phase $\Delta\phi/\pi$ as well as the driving detuning $\Delta_p/2\pi$ with $g_{20}/2\pi = 7.8$ MHz, corresponding to the cavity detuning (c) $\Delta_c/2\pi = 0$ and (d) $\Delta_c/2\pi = 50$ MHz. The color bar on the right-hand side of panels (a)–(d) represent the magnitude of $g^{(2)}(0)$. The other parameters are $\kappa/2\pi = 6.4$ MHz, $\Gamma_{11}/2\pi = 6.1$ MHz, $\Gamma_{22}/2\pi = 5/9 \times 6.1$ MHz, $\Gamma_{12}/2\pi = \sqrt{5/9} \times 6.1$ MHz, $\Omega_{10}/2\pi = 0.65$ MHz, $\eta/2\pi = 0.01$ MHz, and $\Delta/2\pi = 0$ MHz.

the other hand, the above results can operate in the weak-coupling regime [i.e., $g_{20} < (\kappa, \Gamma_1)$, where $\Gamma_1 = \Gamma_{11} + \Gamma_{12}$] [35], which relaxes the requirements on the system parameters and makes the experimental implementation of this scheme more accessible.

On the basis of the previous analysis, in order to more clearly show the influence of the total closed-loop coupling phase $\Delta\phi/\pi$ and the driving detuning $\Delta_p/2\pi$ on the photon statistics of the ONF cavity QED system, we plot the two-dimensional color-scale map of the normalized equal-time second-order intensity correlation function $g^{(2)}(0)$ as a function of the total closed-loop coupling phase $\Delta\phi/\pi$ as well as the driving detuning $\Delta_p/2\pi$ with $g_{20}/2\pi = 2.9$ MHz in Figs. 5(a) and 5(b), corresponding to the two different cases of $\Delta_c/2\pi = 0$ [see Fig. 5(a)] and $\Delta_c/2\pi = 50$ MHz [see Fig. 5(b)]. From Figs. 5(a) and 5(b), one can observe that the transformation of photon antibunching (the blue area) to photon bunching (the red area) can be achieved by appropriately adjusting the total closed-loop coupling phase $\Delta\phi/\pi$. In the scenario of the nonresonant case of the control field [i.e., $\Delta_c/2\pi = 50$ MHz; see Fig. 5(b)], a stronger photon antibunching effect [$g^{(2)}(0) \simeq 0.0001$] can occur near $\Delta_p/2\pi = -50$ MHz. With the increase of the cavity-atom coupling strength [i.e., $g_{20}/2\pi = 7.8$ MHz; see Figs. 5(c) and 5(d)], entering into the strong-coupling regime (i.e., $g_{20} > \kappa$), the

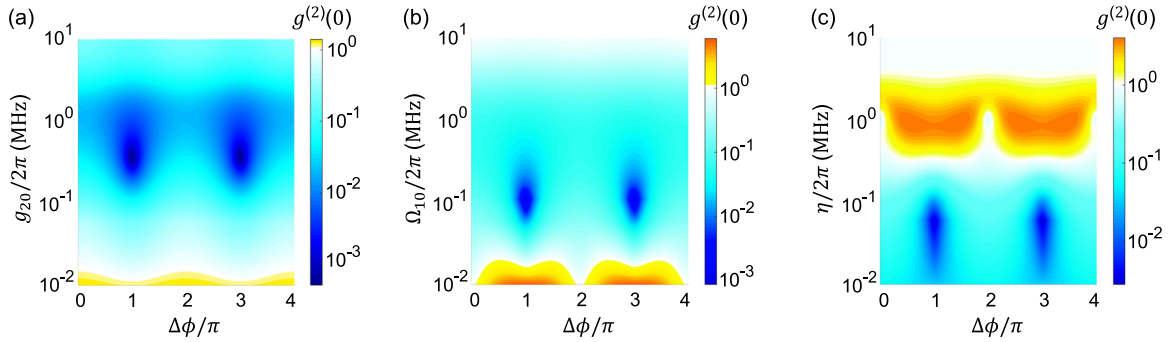


FIG. 6. (a) Contour plot of the normalized equal-time second-order intensity correlation function $g^{(2)}(0)$ as a function of the total closed-loop coupling phase $\Delta\phi/\pi$ as well as the cavity-atom coupling strength $g_{20}/2\pi$ with $\Omega_{10}/2\pi = 0.65$ MHz and $\eta/2\pi = 0.01$ MHz. (b) Contour plot of the normalized equal-time second-order intensity correlation function $g^{(2)}(0)$ as a function of the total closed-loop coupling phase $\Delta\phi/\pi$ as well as the control-field Rabi frequency $\Omega_{10}/2\pi$ with $g_{20}/2\pi = 2.9$ MHz and $\eta/2\pi = 0.01$ MHz. (c) Contour plot of the normalized equal-time second-order intensity correlation function $g^{(2)}(0)$ as a function of the total closed-loop coupling phase $\Delta\phi/\pi$ as well as the driving strength $\eta/2\pi$ with $g_{20}/2\pi = 2.9$ MHz and $\Omega_{10}/2\pi = 0.65$ MHz. The color bar on the right-hand side of panels (a)–(c) represents the magnitude of $g^{(2)}(0)$. The other parameters are $\kappa/2\pi = 6.4$ MHz, $\Gamma_{11}/2\pi = 6.1$ MHz, $\Gamma_{22}/2\pi = 5/9 \times 6.1$ MHz, $\Gamma_{12}/2\pi = \sqrt{5/9} \times 6.1$ MHz, $\Delta_p/2\pi = 0$ MHz, $\Delta/2\pi = 0$ MHz, and $\Delta_c/2\pi = 0$ MHz.

photon bunching effect in the ONF cavity QED system is considerably suppressed (the decrease of the red area), while the photon antibunching effect is enhanced (the increase of the dark blue area). Physically, the two-photon transition pathways in Fig. 4 can be impacted by choosing the different cavity-atom coupling strength $g_{20}/2\pi$ and cavity detuning $\Delta_c/2\pi$, as can be seen from Eqs. (9)–(12). This gives rise to the occurrence of the destructive quantum interference between the different quantum transition pathways under different conditions of $g_{20}/2\pi$ and $\Delta_c/2\pi$, thereby affecting the photon antibunching effect. The strong photon antibunching can be achieved in a broad parameter region [see Figs. 5(c) and 5(d)], which is useful for engineering a tunable single-photon sources. When $\Delta_c/2\pi = 0$ [see Figs. 5(a) and 5(c)], the strong antibunching (the dark blue area) can be observed around $\Delta_p/2\pi = 0$. Alternatively, when $\Delta_c/2\pi = 50$ MHz [see Figs. 5(b) and 5(d)], the strong antibunching (the dark blue area) can be observed around $\Delta_p/2\pi = -50$ MHz. This pronounced antibunching can occur in both resonant case [see Figs. 5(a) and 5(c)] and nonresonant case [see Figs. 5(b) and 5(d)], which can relax the requirements on the system parameters and may have potential applications in quantum information processing and quantum communications [87,88].

Now we explore how the cavity-atom coupling strength $g_{20}/2\pi$, the control-field Rabi frequency $\Omega_{10}/2\pi$, and the driving strength $\eta/2\pi$ affect the statistical property of the ONF cavity QED system. Based on the numerical approach given by the quantum master equation (3), we plot the two-dimensional color-scale map of the normalized equal-time second-order intensity correlation function $g^{(2)}(0)$ in Fig. 6. It can be clearly seen from Figs. 6(a) and 6(b) that the photon antibunching can occur at a certain cavity-atom coupling strength $g_{20}/2\pi$ and control-field Rabi frequency $\Omega_{10}/2\pi$ (the blue area), while the photon bunching exists at a weak cavity-atom coupling strength $g_{20}/2\pi$ and control-field Rabi frequency $\Omega_{10}/2\pi$ (the yellow and red areas). This implies that the occurrence of the destructive quantum interference between the different transition pathways (see Fig. 4) requires

the system to satisfy a certain cavity-atom coupling strength $g_{20}/2\pi$ and control-field Rabi frequency $\Omega_{10}/2\pi$. Conversely, in looking at the result of Fig. 6(c), we find that the photon antibunching can occur at a weak-driving strength $\eta/2\pi$ (the blue area), while the photon bunching exists at a certain driving strength $\eta/2\pi$ (the yellow and red areas). In the weak driving regime, the multiphoton states are rarely excited and the multiphoton events are suppressed, leading to the occurrence of the photon antibunching (the blue area). In the case of the strong driving, the multiphoton states have an important impact on the photon statistical properties of the system, resulting in the occurrence of the photon bunching (the yellow and red areas) when the ONF cavity QED system goes beyond the weak drive limit. The impact of the multiphoton states on the photon statistical properties of the system under different driving conditions will be demonstrated in Appendix D. By tuning both the cavity-atom coupling strength $g_{20}/2\pi$, the control-field Rabi frequency $\Omega_{10}/2\pi$, the driving strength $\eta/2\pi$ and the total closed-loop coupling phase $\Delta\phi/\pi$ appropriately, the strong photon antibunching (the dark blue area) can be well generated in the present ONF cavity QED system.

VI. CONCLUSIONS

In summary, we have demonstrated a feasible phase-engineered scheme for realizing strong photon antibunching accompanying with large brightness in a coupled ONF cavity QED system with the VIC. By tuning the total closed-loop coupling phase adhering on the VIC, quantum correlations of photons can be well tuned from antibunching to bunching regimes. We find that 1PB, 2PB, and PIT can be achieved by adjusting the total closed-loop coupling phase appropriately. We have also investigated the deviations of the photon population and the standard Poisson distribution, whose results also demonstrated that the 2PB effect can occur in our scheme. Moreover, it is possible to obtain the switch from 1PB to 2PB and the switch from 2PB to PIT. Due to (i) the destructive interference between different transition pathways for the two-photon excitation and (ii) the total closed-loop

coupling phase induced by the VIC, a strong photon antibunching can be generated even within the weak-coupling “bad-cavity” regime (without the need of the strong-coupling condition), which relaxes the requirements on the system parameters and makes the experimental implementation of this scheme more accessible. In this regime, the enhanced photon antibunching can occur concurrently with high brightness in the ONF cavity QED system, offering a guiding significance for practical experimental design to a certain extent. Furthermore, we find that the strong photon antibunching can be achieved in a broad parameter region of driving detuning, which can relax the requirement for the driving frequency in the ONF cavity QED system. In addition, we compare the analytical solutions of the second-order and third-order intensity correlation functions with the numerical solutions and find that the agreement between them is reasonably good. We also address the experimental feasibility of the present phase-engineered scheme with existing state-of-the-art ONF cavity QED architecture. The obtained results may be meaningful in engineering single-photon sources [89,90]. Single-photon sources are the basic units of quantum communication. Its strong security and low susceptibility to interference are therefore considered very important in quantum communication [91]. Single-photon sources can also be used in the fields such as quantum imaging and quantum sensing, serving as carriers of quantum information and playing a fundamental role in achieving higher-level quantum technology [92].

ACKNOWLEDGMENTS

We are grateful to X.-Y. Lü and R. Yu for stimulating discussions. The present research is supported partially by the National Natural Science Foundation of China (NSFC) through Grant No. 12275092 and by the National Key Research and Development Program of China under Contract No. 2021YFA1400700.

APPENDIX A: COMPARISON BETWEEN CORRELATION $g^{(2)}(0)$ VERSUS PHASE $\Delta\phi$ WITH AND WITHOUT THE VIC

By applying a unitary transformation to a rotating coordinate frame, we can rewrite the total Hamiltonian \hat{H}_{tot} of Eq. (1) in the main text as

$$\begin{aligned} \hat{H}_{\text{tot}} = & \Delta_p \hat{a}^\dagger \hat{a} + \Delta \hat{\sigma}_{11} + (\Delta_p + \Delta_c) \hat{\sigma}_{22} + (g_{20} e^{i\phi_{20}} \hat{a} \hat{\sigma}_{02}^\dagger \\ & + \Omega_{10} e^{i\phi_{10}} \hat{\sigma}_{01}^\dagger + i\eta \hat{a}^\dagger + \text{H.c.}), \end{aligned} \quad (\text{A1})$$

which is exactly Eq. (2) in the main text. By transforming $\hat{\sigma}_{01} \rightarrow \hat{\sigma}_{01} e^{i\phi_{10}}$ and $\hat{\sigma}_{02} \rightarrow \hat{\sigma}_{02} e^{i\phi_{20}}$, the total closed-loop coupling phase $\Delta\phi = \phi_{10} - \phi_{20}$ can adhere on the VIC and the quantum master equation (3) in the main text can be obtained. To illustrate the photon statistical properties of the ONF cavity QED system varying with the total closed-loop coupling phase $\Delta\phi$ under both the presence and absence of the VIC, we can also transfer the total closed-loop coupling phase $\Delta\phi$ to the cavity-atom coupling strength g_{20} .

Based on the closed-loop transitions $|0\rangle \xleftrightarrow{\Omega_{10} e^{i\phi_{10}}} |1\rangle \xleftrightarrow{\Gamma_{12}} |2\rangle \xleftrightarrow{g_{20} e^{i\phi_{20}}} |0\rangle$ (see the top-right inset of Fig. 1), we can set the

transformation $|0\rangle \rightarrow |0\rangle e^{i\phi_{10}}$, and then the Lindblad master equation can be expressed as

$$\begin{aligned} \frac{\partial \hat{\rho}}{\partial t} = & -i[\hat{H}'_{\text{tra}}, \hat{\rho}] + \kappa \mathcal{D}(\hat{a})\hat{\rho} + \Gamma_{11} \mathcal{D}(\hat{\sigma}_{01})\hat{\rho} + \Gamma_{22} \mathcal{D}(\hat{\sigma}_{02})\hat{\rho} \\ & + \Gamma_{12}(\hat{\sigma}_{01} \hat{\rho} \hat{\sigma}_{02}^\dagger - \hat{\sigma}_{02}^\dagger \hat{\sigma}_{01} \hat{\rho} / 2 - \hat{\rho} \hat{\sigma}_{02}^\dagger \hat{\sigma}_{01} / 2) \\ & + \Gamma_{12}(\hat{\sigma}_{02} \hat{\rho} \hat{\sigma}_{01}^\dagger - \hat{\sigma}_{01}^\dagger \hat{\sigma}_{02} \hat{\rho} / 2 - \hat{\rho} \hat{\sigma}_{01}^\dagger \hat{\sigma}_{02} / 2), \end{aligned} \quad (\text{A2})$$

with

$$\begin{aligned} \hat{H}'_{\text{tra}} = & \Delta_p \hat{a}^\dagger \hat{a} + \Delta \hat{\sigma}_{11} + (\Delta_p + \Delta_c) \hat{\sigma}_{22} + (g_{20} e^{-i\Delta\phi} \hat{a} \hat{\sigma}_{02}^\dagger \\ & + \Omega_{10} \hat{\sigma}_{01}^\dagger + i\eta \hat{a}^\dagger + \text{H.c.}). \end{aligned} \quad (\text{A3})$$

It is worth emphasizing that the existence of the VIC effect is important for the photon statistical properties of the ONF cavity QED system. In the following, we take Fig. 3(a) as an example and plot the normalized equal-time second-order intensity correlation function $g^{(2)}(0)$ as a function of the total closed-loop coupling phase $\Delta\phi/\pi$ with the VIC (the purple-dotted line) and without the VIC (i.e., $\Gamma_{12} = 0$; the pink-solid line) numerically calculated by the master equation (A2) in Fig. 7. When the VIC is present (the purple-dotted line), quantum correlations of photons can be well tuned from antibunching to bunching regimes by adjusting the total closed-loop coupling phase. On the contrary, in the absence of the VIC (the pink-solid line), the system shows coherent-state photons [i.e., $g^{(2)}(0) = 1$] and the photon antibunching disappears. This is because, in the absence of the VIC, the quantum interference between different pathways of two-photon excitation disappears (see the red double arrows in Fig. 4). At the same time, the closed-loop configuration of the system is destroyed and so the phase-dependent effect disappears.

For two-photon excitation, there exist two different excitation pathways to the two-photon excitation state $|0, 2\rangle$,

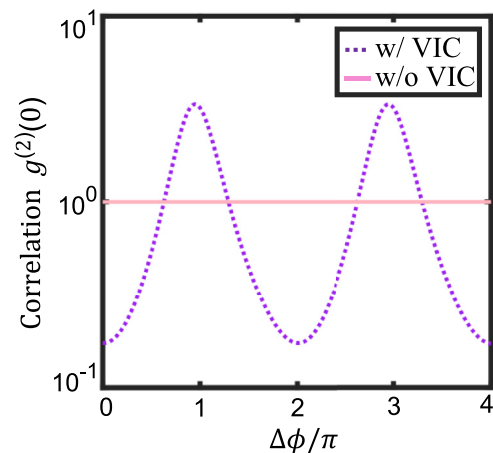


FIG. 7. The normalized equal-time second-order intensity correlation function $g^{(2)}(0)$ as a function of the total closed-loop coupling phase $\Delta\phi/\pi$ with the VIC (the purple-dotted line) and without the VIC (the pink-solid line), numerically calculated by the master equation (A2). The other parameters are $\kappa/2\pi = 6.4$ MHz, $\Gamma_{11}/2\pi = 6.1$ MHz, $\Gamma_{22}/2\pi = 5/9 \times 6.1$ MHz, $\Gamma_{12}/2\pi = \sqrt{5/9} \times 6.1$ MHz, $g_{20}/2\pi = 2.9$ MHz, $\Omega_{10}/2\pi = 0.65$ MHz, $\eta/2\pi = 0.01$ MHz, $\Delta_p/2\pi = -36$ MHz, $\Delta/2\pi = 10$ MHz, and $\Delta_c/2\pi = 20$ MHz.

that is to say, direct pathway (i) $|0, 0\rangle \xrightarrow{\eta} |0, 1\rangle \xrightarrow{\sqrt{2}\eta} |0, 2\rangle$ and indirect pathway (ii) $|0, 0\rangle \xrightarrow{\Omega_{10}} |1, 0\rangle \xrightarrow{\eta} |1, 1\rangle \xrightarrow{\Gamma_{12}e^{i\Delta\phi}/2} |2, 1\rangle \xrightarrow{\sqrt{2}g_{20}} |0, 2\rangle$ (see Fig. 4). The introduction of the VIC (i.e., Γ_{12}) has an important influence on the indirect pathway (i.e., $|1, 1\rangle \xrightarrow{\Gamma_{12}e^{i\Delta\phi}/2} |2, 1\rangle$); see the red double arrows in Fig. 4, thereby affecting the quantum interference between different pathways of two-photon excitation. To intuitively analyze the influence of introducing the VIC, we can obtain the probabilities $|C_{11}|^2$ and $|C_{21}|^2$ corresponding to the states $|1, 1\rangle$ and $|2, 1\rangle$ through numerical calculations. As an example, when $\Delta\phi = 0$ (see Fig. 7), in the presence of the VIC, the probabilities are $|C_{11}|^2 = 3.8 \times 10^{-11}$ and $|C_{21}|^2 = 3.4 \times 10^{-12}$, representing that the probability of the state $|2, 1\rangle$ is only one order of magnitude smaller than that of the state $|1, 1\rangle$. In contrast, in the absence of the VIC, the probabilities are $|C_{11}|^2 = 2.9 \times 10^{-10}$ and $|C_{21}|^2 = 2.0 \times 10^{-16}$, where the probability of the state $|2, 1\rangle$ is six orders of magnitude smaller than that of the state $|1, 1\rangle$. From the results mentioned above, we can see that the introduction of the VIC bridges the indirect pathway $|1, 1\rangle \xrightarrow{\Gamma_{12}e^{i\Delta\phi}/2} |2, 1\rangle$, enabling the transfer of photons from state $|1, 1\rangle$ to state $|2, 1\rangle$. By introducing the VIC, the quantum interference between different pathways of two-photon excitation can be generated and the photon antibunching can be achieved, which may be useful for the energy-transfer studies [4–6].

APPENDIX B: ANALYTICAL SOLUTIONS OF THE SECOND-ORDER INTENSITY CORRELATION FUNCTION IN THE WEAK-DRIVING LIMIT VIA THE SCHRÖDINGER EQUATION APPROACH

In this Appendix, we present approximate analytical expressions for the phase-sensitive equal-time second-order intensity correlation function as an alternative method to characterize the photon statistical properties of the ONF cavity QED system. The quantum state of the system can be represented as an expansion based on a Fock state basis. Under the condition that the external driving laser field is very weak (i.e., $\eta \ll g_{20}, \kappa$), the population of the high-photon excitation states is very low, thus it can be assumed that the total excitation number of the ONF cavity QED system is no more than two [21,22]. Consequently, the wave function of the ONF cavity QED system can be reasonably approximated in the two-excitation manifold with the ansatz [21,93]

$$|\Psi(t)\rangle \simeq C_{00}|0, 0\rangle + C_{01}|0, 1\rangle + C_{02}|0, 2\rangle + C_{10}|1, 0\rangle + C_{11}|1, 1\rangle + C_{20}|2, 0\rangle + C_{21}|2, 1\rangle, \quad (\text{B1})$$

where the state $|j, n\rangle = |j\rangle \otimes |n\rangle$ means the three-level atom in the state of $|j\rangle$ ($j = 0, 1, 2$) and the Fock basis for the cavity mode with the photon number n ($n = 0, 1, 2$). Here the coefficient C_{jn} represents the probability amplitude of the corresponding state $|j, n\rangle$, for which the corresponding probability is given by $|C_{jn}|^2$. In the weak-driving regime, the system is rarely in an excited state and thus the $\hat{a}\hat{\rho}\hat{a}^\dagger$ and $\hat{\sigma}_{lm}\hat{\rho}\hat{\sigma}_{lm}^\dagger$ ($l, m = 0, 1, 2$) terms in the Lindblad master equation can be neglected [94–96]. When they are removed,

the Lindblad master equation (3) is equivalent to the time-dependent Schrödinger equation

$$i\frac{\partial|\Psi\rangle}{\partial t} = \hat{H}_{\text{eff}}|\Psi\rangle, \quad (\text{B2})$$

with

$$\begin{aligned} \hat{H}_{\text{eff}} = & (\Delta_p - i\kappa/2)\hat{a}^\dagger\hat{a} + (\Delta - i\Gamma_{11}/2)\hat{\sigma}_{11} \\ & + (\Delta_p + \Delta_c - i\Gamma_{22}/2)\hat{\sigma}_{22} \\ & - i\Gamma_{12}(e^{i\Delta\phi}\hat{\sigma}_{21} + e^{-i\Delta\phi}\hat{\sigma}_{12})/2 \\ & + (g_{20}\hat{a}\hat{\sigma}_{02}^\dagger + \Omega_{10}\hat{\sigma}_{01}^\dagger + i\eta\hat{a}^\dagger + \text{H.c.}), \end{aligned} \quad (\text{B3})$$

where the effective non-Hermitian Hamiltonian \hat{H}_{eff} contains the optical cavity damping and three-level atomic damping terms in addition to the original Hamiltonian (4) and whose steady-state solution yields the photon statistics of the ONF cavity QED system for zero time delay. More concretely, the imaginary part (characterizes the dissipative coupling) of the first term on the RHS of Eq. (B3) denotes that the coupling of the cavity with a reservoir results in the damping κ . The imaginary parts of the second and third terms on the RHS of Eq. (B3) represent that the coupling of the two quantum transition pathways with a common reservoir results in the damping rates Γ_{11} and Γ_{22} , respectively. Finally, the imaginary part of the fourth term (i.e., the VIC between both radiative channels) on the RHS of Eq. (B3) indicates that the coupling with the common reservoir induces a dissipative coupling $\Gamma_{12} \simeq \sqrt{\Gamma_{11}\Gamma_{22}}$ between these two radiative channels [7], which is impacted by the total closed-loop coupling phase $\Delta\phi$.

By substituting the wave function of the ONF cavity QED system $|\Psi(t)\rangle$ [Eq. (B1)] and the effective non-Hermitian Hamiltonian \hat{H}_{eff} [Eq. (B3)] into the Schrödinger equation (B2), the above coefficients C_{jn} satisfy the equations of motion (overdots indicate time derivatives)

$$i\dot{C}_{00} = \Omega_{10}C_{10} - i\eta^*C_{01}, \quad (\text{B4})$$

$$\begin{aligned} i\dot{C}_{01} = & (\Delta_p - i\kappa/2)C_{01} + g_{20}C_{20} + \Omega_{10}C_{11} \\ & + i\eta C_{00} - i\sqrt{2}\eta^*C_{02}, \end{aligned} \quad (\text{B5})$$

$$i\dot{C}_{02} = 2(\Delta_p - i\kappa/2)C_{02} + \sqrt{2}g_{20}C_{21} + i\sqrt{2}\eta C_{01}, \quad (\text{B6})$$

$$\begin{aligned} i\dot{C}_{10} = & (\Delta - i\Gamma_{11}/2)C_{10} - i\Gamma_{12}e^{-i\Delta\phi}C_{20}/2 \\ & + \Omega_{10}C_{00} - i\eta^*C_{11}, \end{aligned} \quad (\text{B7})$$

$$\begin{aligned} i\dot{C}_{11} = & (\Delta_p + \Delta - i\kappa/2 - i\Gamma_{11}/2)C_{11} \\ & - i\Gamma_{12}e^{-i\Delta\phi}C_{21}/2 + \Omega_{10}C_{01} + i\eta C_{10}, \end{aligned} \quad (\text{B8})$$

$$\begin{aligned} i\dot{C}_{20} = & (\Delta_p + \Delta_c - i\Gamma_{22}/2)C_{20} - i\Gamma_{12}e^{i\Delta\phi}C_{10}/2 \\ & + g_{20}C_{01} - i\eta^*C_{21}, \end{aligned} \quad (\text{B9})$$

$$\begin{aligned} i\dot{C}_{21} = & (2\Delta_p + \Delta_c - i\kappa/2 - i\Gamma_{22}/2)C_{21} \\ & - i\Gamma_{12}e^{i\Delta\phi}C_{11}/2 + \sqrt{2}g_{20}C_{02} + i\eta C_{20}. \end{aligned} \quad (\text{B10})$$

For the case of the one-photon and two-photon states, in the steady state $\dot{C}_{jn} = 0$, the equations for the coefficients C_{jn} can

be written as

$$0 = (\Delta_p - i\kappa/2)C_{01} + g_{20}C_{20} + \Omega_{10}C_{11} + i\eta C_{00} - i\sqrt{2}\eta^*C_{02}, \quad (\text{B11})$$

$$0 = 2(\Delta_p - i\kappa/2)C_{02} + \sqrt{2}g_{20}C_{21} + i\sqrt{2}\eta C_{01}, \quad (\text{B12})$$

$$0 = (\Delta - i\Gamma_{11}/2)C_{10} - i\Gamma_{12}e^{-i\Delta\phi}C_{20}/2 + \Omega_{10}C_{00} - i\eta^*C_{11}, \quad (\text{B13})$$

$$0 = (\Delta_p + \Delta - i\kappa/2 - i\Gamma_{11}/2)C_{11} - i\Gamma_{12}e^{-i\Delta\phi}C_{21}/2 + \Omega_{10}C_{01} + i\eta C_{10}, \quad (\text{B14})$$

$$0 = (\Delta_p + \Delta_c - i\Gamma_{22}/2)C_{20} - i\Gamma_{12}e^{i\Delta\phi}C_{10}/2 + g_{20}C_{01} - i\eta^*C_{21}, \quad (\text{B15})$$

$$0 = (2\Delta_p + \Delta_c - i\kappa/2 - i\Gamma_{22}/2)C_{21} - i\Gamma_{12}e^{i\Delta\phi}C_{11}/2 + \sqrt{2}g_{20}C_{02} + i\eta C_{20}. \quad (\text{B16})$$

The coefficients C_{jn} can be iteratively calculated by solving the above coupled algebraic equations (B11)–(B16). In the limit of weak driving, for the probability amplitude coefficients C_{jn} we have the relationship $C_{00} \gg \{C_{01}, C_{10}, C_{20}\} \gg \{C_{02}, C_{11}, C_{21}\}$. Furthermore, like previous works [97,98], it is reasonable to make the assumption that the vacuum state is approximately occupied with probability one. In this regard, we can assume $C_{00} \approx 1$, $\eta C_{02} \approx 0$, $\eta C_{11} \approx 0$, and $\eta C_{21} \approx 0$. Due to the verbosity of the solutions for the coefficients C_{jn} , only $C_{01}[\Delta\phi]$ and $C_{02}[\Delta\phi]$ ($[\Delta\phi]$ represents that C_{01} and C_{02} are functions related to $\Delta\phi$) are given by

$$C_{01}[\Delta\phi] = \frac{ie^{i\Delta\phi}[2e^{i\Delta\phi}g_{20}\Omega_{10}\Gamma_{12}(4X_{01} + \Delta'_p\Gamma_{12}^2) + \eta(-16\Delta'_c Y_{01} + 4Z_{01}\Gamma_{12}^2 - \Delta'_p\Gamma_{12}^4)]}{2g_{20}\eta\Omega_{10}\Gamma_{12}(A - \Gamma_{12}^2) + e^{i\Delta\phi}(16\Delta'B + 4C\Gamma_{12}^2 + \Delta_p'^2\Gamma_{12}^4)}, \quad (\text{B17})$$

$$C_{02}[\Delta\phi] = \frac{-4e^{3i\Delta\phi}g_{20}^2\Omega_{10}^2\Gamma_{12}^2 - 4e^{2i\Delta\phi}g_{20}\eta\Omega_{10}\Gamma_{12}(2X_{02} - \Gamma_{12}^2) - e^{i\Delta\phi}\eta^2(16Y_{02} + 4Z_{02}\Gamma_{12}^2 + \Gamma_{12}^4)}{\sqrt{2}[2g_{20}\eta\Omega_{10}\Gamma_{12}(A - \Gamma_{12}^2) + e^{i\Delta\phi}(16\Delta'B + 4C\Gamma_{12}^2 + \Delta_p'^2\Gamma_{12}^4)]}, \quad (\text{B18})$$

where

$$\begin{aligned} A &= 4g_{20}^2 - 4(\Delta'_p + \Delta')(\Delta'_p + \Delta'_c), \\ B &= [g_{20}^2 - \Delta'_p(\Delta'_p + \Delta'_c)][\Omega_{10}^2\Delta'_c + (\Delta'_p + \Delta')(g_{20}^2 - \Delta'_p\Delta'_c)], \\ C &= \Delta'_p\Delta'(-2g_{20}^2 + 2\Delta'_p\Delta'_c + \Delta_p'^2) - (\Omega_{10} - \Delta'_p)(\Omega_{10} + \Delta'_p)[-g_{20}^2 + \Delta'_p(\Delta'_p + \Delta'_c)], \\ X_{01} &= (\Delta'_p + \Delta')[-g_{20}^2 + \Delta'_p(\Delta'_p + \Delta'_c)], \\ Y_{01} &= [\Omega_{10}^2 + \Delta'(\Delta'_p + \Delta')][-g_{20}^2 + \Delta'_p(\Delta'_p + \Delta'_c)], \\ Z_{01} &= \Delta'_p[g_{20}^2 + \Omega_{10}^2 - \Delta'_p(\Delta'_p + \Delta'_c)] + \Delta'[g_{20}^2 - \Delta'_p(\Delta'_p + 2\Delta'_c)], \\ X_{02} &= g_{20}^2 + \Omega_{10}^2 - 2(\Delta'_p + \Delta')(\Delta'_p + \Delta'_c), \\ Y_{02} &= [\Omega_{10}^2 + \Delta'(\Delta'_p + \Delta')][g_{20}^2 + \Delta'_c(\Delta'_p + \Delta'_c)], \\ Z_{02} &= -g_{20}^2 - \Omega_{10}^2 + \Delta'_p(\Delta'_p + \Delta'_c) + \Delta'(\Delta'_p + 2\Delta'_c), \end{aligned} \quad (\text{B19})$$

with $\Delta'_p = \Delta_p - i\kappa/2$, $\Delta' = \Delta - i\Gamma_{11}/2$, and $\Delta'_c = \Delta_p + \Delta_c - i\Gamma_{22}/2$.

The other coefficients C_{jn} can also be solved using the same method; however, for the sake of simplicity, they are not presented here. Based on the solutions for the probability amplitude coefficients $C_{01}[\Delta\phi]$ [Eq. (B17)] and $C_{02}[\Delta\phi]$ [Eq. (B18)] in Eq. (B1), the normalized equal-time second-order intensity correlation function $g^{(2)}(0)[\Delta\phi]$ can be further expressed as

$$g^{(2)}(0)[\Delta\phi] = \frac{\langle \Psi | \hat{a}^\dagger \hat{a}^\dagger \hat{a} \hat{a} | \Psi \rangle_{ss}}{(\langle \Psi | \hat{a}^\dagger \hat{a} | \Psi \rangle_{ss})^2} \simeq \frac{2|C_{02}[\Delta\phi]|^2}{|C_{01}[\Delta\phi]|^4}, \quad (\text{B20})$$

where the subscript ‘‘ss’’ indicates the expectation values taken with respect to the steady-state solution, accordingly $|\Psi\rangle$ represents the steady-state wave function of the ONF cavity QED system. From the derivations presented above [i.e., Eqs. (B17)–(B20)], we can see that the normalized equal-time second-order intensity correlation function $g^{(2)}(0)[\Delta\phi]$ is closely related to both the VIC (i.e., Γ_{12}) and the total closed-loop coupling phase $\Delta\phi$, playing an important role

in generating strong antibunching for the ONF cavity QED system.

APPENDIX C: ANALYTICAL SOLUTIONS OF THE THIRD-ORDER INTENSITY CORRELATION FUNCTION IN THE WEAK-DRIVING LIMIT VIA THE SCHRÖDINGER EQUATION APPROACH

In the regime of weak driving, for a clearer and more concise presentation of the explicit expressions for the probability amplitude coefficients $C_{01}[\Delta\phi]$ and $C_{02}[\Delta\phi]$, we only truncate the wave function of the ONF cavity QED system to the two-excitation manifold, as mentioned above in Appendix B. This truncation provides a clearer insight into the effects of the VIC and the total closed-loop coupling phase on the second-order intensity correlation function. In this Appendix, we present here approximate analytical solution for the equal-time third-order intensity correlation function. Alternatively,

the wave function of the ONF cavity QED system under weak-driving condition can be reasonably approximated in the three-excitation manifold with the ansatz

$$\begin{aligned}
 |\Psi(t)\rangle \simeq & C_{00}|0, 0\rangle + C_{01}|0, 1\rangle + C_{02}|0, 2\rangle + C_{03}|0, 3\rangle \\
 & + C_{10}|1, 0\rangle + C_{11}|1, 1\rangle + C_{12}|1, 2\rangle \\
 & + C_{20}|2, 0\rangle + C_{21}|2, 1\rangle + C_{22}|2, 2\rangle. \quad (\text{C1})
 \end{aligned}$$

In the same manner as Appendix B, the coefficients C_{jn} ($j, n = 0, 1, 2, 3$, similar to the definition in Appendix B) of the one-photon, two-photon, and three-photon states are determined by

$$\begin{aligned}
 0 = & (\Delta_p - ik/2)C_{01} + g_{20}C_{20} + \Omega_{10}C_{11} + i\eta C_{00} \\
 & - i\sqrt{2}\eta^*C_{02}, \quad (\text{C2})
 \end{aligned}$$

$$\begin{aligned}
 0 = & 2(\Delta_p - ik/2)C_{02} + \sqrt{2}g_{20}C_{21} + \Omega_{10}C_{12} \\
 & + i\sqrt{2}\eta C_{01} - i\sqrt{3}\eta^*C_{03}, \quad (\text{C3})
 \end{aligned}$$

$$0 = 3(\Delta_p - ik/2)C_{03} + \sqrt{3}g_{20}C_{22} + i\sqrt{3}\eta C_{02}, \quad (\text{C4})$$

$$\begin{aligned}
 0 = & (\Delta - i\Gamma_{11}/2)C_{10} - i\Gamma_{12}e^{-i\Delta\phi}C_{20}/2 + \Omega_{10}C_{00} \\
 & - i\eta^*C_{11}, \quad (\text{C5})
 \end{aligned}$$

$$\begin{aligned}
 0 = & (\Delta_p + \Delta - ik/2 - i\Gamma_{11}/2)C_{11} - i\Gamma_{12}e^{-i\Delta\phi}C_{21}/2 \\
 & + \Omega_{10}C_{01} + i\eta C_{10} - i\sqrt{2}\eta^*C_{12}, \quad (\text{C6})
 \end{aligned}$$

$$\begin{aligned}
 0 = & (2\Delta_p + \Delta - ik - i\Gamma_{11}/2)C_{12} - i\Gamma_{12}e^{-i\Delta\phi}C_{22}/2 \\
 & + \Omega_{10}C_{02} + i\sqrt{2}\eta C_{11}, \quad (\text{C7})
 \end{aligned}$$

$$\begin{aligned}
 0 = & (\Delta_p + \Delta_c - i\Gamma_{22}/2)C_{20} - i\Gamma_{12}e^{i\Delta\phi}C_{10}/2 \\
 & + g_{20}C_{01} - i\eta^*C_{21}, \quad (\text{C8})
 \end{aligned}$$

$$\begin{aligned}
 0 = & (2\Delta_p + \Delta_c - ik/2 - i\Gamma_{22}/2)C_{21} - i\Gamma_{12}e^{i\Delta\phi}C_{11}/2 \\
 & + \sqrt{2}g_{20}C_{02} + i\eta C_{20} - i\sqrt{2}\eta^*C_{22}, \quad (\text{C9})
 \end{aligned}$$

$$\begin{aligned}
 0 = & (3\Delta_p + \Delta_c - ik - i\Gamma_{22}/2)C_{22} - i\Gamma_{12}e^{i\Delta\phi}C_{12}/2 \\
 & + \sqrt{3}g_{20}C_{03} + i\sqrt{2}\eta C_{21}. \quad (\text{C10})
 \end{aligned}$$

Under the condition of weak driving, we have the relationship $C_{00} \gg \{C_{01}, C_{10}, C_{20}\} \gg \{C_{02}, C_{11}, C_{21}\} \gg \{C_{03}, C_{12}, C_{22}\}$ and thus we can assume $C_{00} \approx 1$. In principle, the coefficients C_{jn} can be obtained by directly solving the above coupled algebraic equations (C2)–(C10). However, the explicit expressions for the probability amplitude coefficients C_{jn} are too long and bulky to be included here. In terms of the coefficients C_{jn} , the normalized equal-time third-order intensity correlation function $g^{(3)}(0)[\Delta\phi]$ can be further expressed as

$$\begin{aligned}
 g^{(3)}(0)[\Delta\phi] &= \frac{\langle \Psi | \hat{a}^\dagger \hat{a}^\dagger \hat{a}^\dagger \hat{a} \hat{a} \hat{a} | \Psi \rangle_{ss}}{\langle \Psi | \hat{a}^\dagger \hat{a} | \Psi \rangle_{ss}^3} \\
 &\simeq \frac{6|C_{03}[\Delta\phi]|^2}{|C_{01}[\Delta\phi]|^6}, \quad (\text{C11})
 \end{aligned}$$

where the subscript “ss” indicates the expectation values taken with respect to the steady-state solution, accordingly $|\Psi\rangle$ represents the steady-state wave function of the ONF cavity QED system.

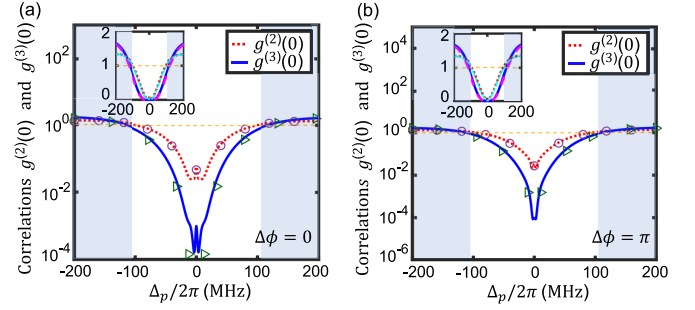


FIG. 8. The normalized equal-time second- and third-order intensity correlation functions $g^{(2)}(0)$ (the red-dotted lines) and $g^{(3)}(0)$ (the blue-solid lines) as a function of the driving detuning $\Delta_p/2\pi$, corresponding to the two different total closed-loop coupling phases (a) $\Delta\phi = 0$ and (b) $\Delta\phi = \pi$. The red-dotted lines and the blue-solid lines are the numerical results calculated directly by the quantum master equation (3). The purple circles are the analytical results of $g^{(2)}(0)$ calculated by the closed-form expressions (9)–(12) and the green triangles are the analytical results of $g^{(3)}(0)$ calculated by the closed-form expression (C11). The comparisons between the numerical results (the red-dotted lines and the blue-solid lines) and the analytical results [cyan-dash-dotted lines (i.e., the purple circles) and magenta-dashed lines (i.e., the green triangles)] are also shown in the insets, where the insets use the normal vertical axis to better display the fitting results. The blue area in panels (a) and (b) indicate the photon bunching. The other parameters are $\kappa/2\pi = 6.4$ MHz, $\Gamma_{11}/2\pi = 6.1$ MHz, $\Gamma_{22}/2\pi = 5/9 \times 6.1$ MHz, $\Gamma_{12}/2\pi = \sqrt{5/9} \times 6.1$ MHz, $g_{20}/2\pi = 2.9$ MHz, $\Omega_{10}/2\pi = 0.65$ MHz, $\eta/2\pi = 0.01$ MHz, $\Delta/2\pi = 0$ MHz, and $\Delta_c/2\pi = 0$ MHz.

APPENDIX D: ANALYSIS OF THE SLIGHT DISCREPANCY BETWEEN THE ANALYTICAL AND NUMERICAL RESULTS

In this Appendix, we mainly focus on how the slight discrepancy between the analytical and numerical results arises. Before proceeding, according to Fig. 2 in the main text, it can be observed that the switching between bunching and antibunching can be realized by adjusting the total closed-loop coupling phase. It is worth emphasizing that the switching between bunching and antibunching can also be realized by adjusting the driving detuning. In what follows, we take Figs. 2(a) and 2(c) as examples and plot the normalized equal-time second- and third-order intensity correlation functions $g^{(2)}(0)$ (the red-dotted lines) and $g^{(3)}(0)$ (the blue-solid lines) as a function of the driving detuning $\Delta_p/2\pi$ in a broader parameter region in Fig. 8, corresponding to the two different total closed-loop coupling phases $\Delta\phi = \{0, \pi\}$. The blue area in Fig. 8 represents the photon bunching [i.e., $g^{(2)}(0) > 1$]. It can be seen from Fig. 8 that the photon bunching (the blue area) can occur at $\Delta\phi = \{0, \pi\}$ as the driving detuning $\Delta_p/2\pi$ increases. As compared with Figs. 2(b) and 2(d) (i.e., $\Delta\phi = \{\pi/2, 3\pi/2\}$), the photon bunching effect at $\Delta\phi = \{0, \pi\}$ [the blue area in Figs. 8(a) and 8(b)] is relatively weak. This implies that the joint regulation of the driving frequency and the total closed-loop coupling phase can better realize the switching between bunching and antibunching in the ONF cavity QED system.

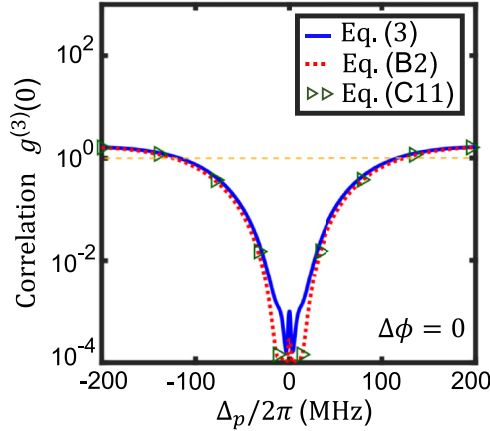


FIG. 9. The normalized equal-time third-order intensity correlation function $g^{(3)}(0)$ as a function of the driving detuning $\Delta_p/2\pi$. The blue-solid line is the numerical result calculated directly by the quantum master equation (3) within a truncated Fock space at photon number as low as 10 (i.e., the truncated photon number $N = 10$) for the ONF cavity mode. The red-dotted line is the numerical result calculated directly by the Schrödinger equation (B2) within the truncated photon number $N = 10$. The green triangles are the analytical result calculated by the closed-form expression (C11). The other parameters are $\kappa/2\pi = 6.4$ MHz, $\Gamma_{11}/2\pi = 6.1$ MHz, $\Gamma_{22}/2\pi = 5/9 \times 6.1$ MHz, $\Gamma_{12}/2\pi = \sqrt{5/9} \times 6.1$ MHz, $g_{20}/2\pi = 2.9$ MHz, $\Omega_{10}/2\pi = 0.65$ MHz, $\eta/2\pi = 0.01$ MHz, $\Delta\phi = 0$, $\Delta/2\pi = 0$ MHz, and $\Delta_c/2\pi = 0$ MHz.

In addition, the comparisons between the numerical results (the red-dotted lines and the blue-solid lines) and the analytical results (cyan-dash-dotted lines and magenta-dashed lines) are shown in the insets of Fig. 8, where the insets use the normal vertical axis to better display the fitting results. However, by comparing with the logarithmic plot (of base 10), we can find that a slight discrepancy exists between the analytical and numerical results [e.g., the green triangles and the blue-solid lines in Figs. 2(a) and 8(a)]. The slight discrepancy between the analytical results obtained by the Schrödinger equation (B2) and the numerical results given by the master equation (3) can be primarily attributed to two factors: (i) in the weak-driving regime, the analytical results obtained by the Schrödinger equation ignore the quantum jump terms $\hat{a}\hat{\rho}\hat{a}^\dagger$ and $\hat{\sigma}_{lm}\hat{\rho}\hat{\sigma}_{lm}^\dagger$ ($l, m = 0, 1, 2$) in the Lindblad superoperator [94–96], and (ii) the analytical results obtained by the Schrödinger equation make the truncation approximation [21,22], ignoring the influence of higher-order photons on the correlation functions.

In the following, for the purpose of demonstrating the impact of the quantum jump terms, we plot the normalized equal-time third-order intensity correlation function $g^{(3)}(0)$ as a function of the driving detuning $\Delta_p/2\pi$ at $\Delta\phi = 0$ in Fig. 9, corresponding to numerically calculated by the quantum master equation (3) (the blue-solid line), numerically calculated by the Schrödinger equation (B2) (the red-dotted line), and analytically calculated by the closed-form expression (C11) (the green triangles), respectively. Under the condition of the same truncated photon number $N = 10$, it can be seen from Fig. 9 that there is a slight discrepancy between the numerical result

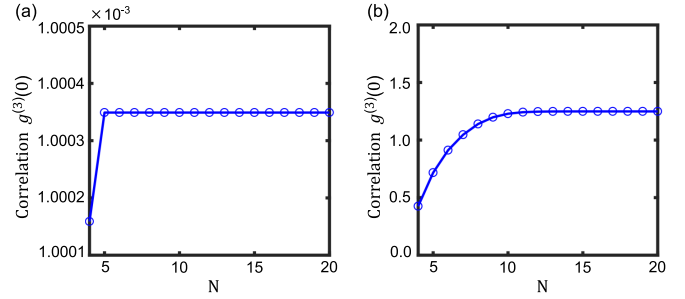


FIG. 10. The normalized equal-time third-order intensity correlation function $g^{(3)}(0)$ as a function of the truncated photon number N , corresponding to the two different driving strengths (a) $\eta/2\pi = 0.01$ MHz and (b) $\eta/2\pi = 5$ MHz. The blue-circle-solid lines are the numerical results calculated directly by the quantum master equation (3) within the truncated photon number N . The other parameters are $\kappa/2\pi = 6.4$ MHz, $\Gamma_{11}/2\pi = 6.1$ MHz, $\Gamma_{22}/2\pi = 5/9 \times 6.1$ MHz, $\Gamma_{12}/2\pi = \sqrt{5/9} \times 6.1$ MHz, $g_{20}/2\pi = 2.9$ MHz, $\Omega_{10}/2\pi = 0.65$ MHz, $\Delta\phi = 0$, $\Delta_p/2\pi = 0$ MHz, $\Delta/2\pi = 0$ MHz, and $\Delta_c/2\pi = 0$ MHz.

(the red-dotted line) calculated directly by the Schrödinger equation (B2) ignoring the quantum jump terms and the numerical result (the blue-solid line) calculated directly by the quantum master equation (3). In the case of ignoring the quantum jump terms, the numerical result (the red-dotted line) calculated directly by the Schrödinger equation (B2) within the truncated photon number $N = 10$ is in good agreement with the analytical result (the green triangles; the truncated photon number $N = 3$) calculated by the closed-form expression (C11). This means that the slight discrepancy between the analytical results obtained by the Schrödinger equation (B2) and the numerical results given by the master equation (3) is primarily attributed to the neglect of the quantum jump terms in the weak-driving regime.

In the weak-driving regime, we take the truncated photon number $N = 10$ to obtain the numerical results given by the master equation (3), while in the strong-driving regime, we take the truncated photon number $N = 20$ for the numerical simulations. The truncated photon numbers for the weak- and strong-driving regimes are sufficient to guarantee the convergence of the numerical simulations. To better demonstrate the convergence of the numerical simulations and the influence of higher-order photons on the correlation functions, we plot the normalized equal-time third-order intensity correlation function $g^{(3)}(0)$ as a function of the truncated photon number N at $\Delta\phi = 0$ and $\Delta_p/2\pi = 0$ in Fig. 10, corresponding to the two different driving strengths $\eta/2\pi = 0.01$ MHz [see Fig. 10(a)] and $\eta/2\pi = 5$ MHz [see Fig. 10(b)]. In the case of weak driving [see Fig. 10(a)], the influence of higher-order photons on the correlation functions (the blue-circle-solid line) is weak and the blue-circle-solid line quickly converges at $N = 5$ (we take $N = 10$ as sufficient), which is consistent with that shown in Fig. 9 (the red-dotted line is in good agreement with the green triangles). From Fig. 10(b), in the strong-driving regime, one can observe that the blue-circle-solid line converges at $N = 12$ (we take $N = 20$ as sufficient). This implies that in the strong-driving regime, higher-order photons have an important impact on the second- and third-order

correlation functions, that is to say, higher-order processes are involved in the 1PB, 2PB, and PIT effects when the

ONF cavity QED system goes beyond the weak-driving limit.

-
- [1] P. Kochan, H. J. Carmichael, P. R. Morrow, and M. G. Raizen, Mutual coherence and interference in resonance fluorescence, *Phys. Rev. Lett.* **75**, 45 (1995).
- [2] M. D. Lukin, P. R. Hemmer, M. Löffler, and M. O. Scully, Resonant enhancement of parametric processes via radiative interference and induced coherence, *Phys. Rev. Lett.* **81**, 2675 (1998).
- [3] X. Wang, J. Wang, Z. Ren, R. Wen, C.-L. Zou, G. A. Siviloglou, and J. F. Chen, Quantum interference between photons and single quanta of stored atomic coherence, *Phys. Rev. Lett.* **128**, 083605 (2022).
- [4] G. S. Agarwal and A. K. Patnaik, Vacuum-induced coherences in radiatively coupled multilevel systems, *Phys. Rev. A* **63**, 043805 (2001).
- [5] J. Evers, M. Kiffner, M. Macovei, and C. H. Keitel, Geometry-dependent dynamics of two Λ -type atoms via vacuum-induced coherences, *Phys. Rev. A* **73**, 023804 (2006).
- [6] S. I. Schmid and J. Evers, Interplay of vacuum-mediated inter- and intra-atomic couplings in a pair of atoms, *Phys. Rev. A* **81**, 063805 (2010).
- [7] H. S. Han, A. Lee, K. Sinha, F. K. Fatemi, and S. L. Rolston, Observation of vacuum-induced collective quantum beats, *Phys. Rev. Lett.* **127**, 073604 (2021); see also accompanying online supplemental material.
- [8] P. Kumar, B. Deb, and S. Dasgupta, Probing vacuum-induced coherence via magneto-optical rotation in molecular systems, *Phys. Rev. A* **93**, 063826 (2016).
- [9] D. A. Cardimona, M. G. Raymer, and C. R. S. Jr, Steady-state quantum interference in resonance fluorescence, *J. Phys. B: At. Mol. Phys.* **15**, 55 (1982).
- [10] P. Zhou and S. Swain, Ultranarrow spectral lines via quantum interference, *Phys. Rev. Lett.* **77**, 3995 (1996).
- [11] P. Zhou and S. Swain, Quantum interference in resonance fluorescence for a driven V atom, *Phys. Rev. A* **56**, 3011 (1997).
- [12] S. Menon and G. S. Agarwal, Effects of spontaneously generated coherence on the pump-probe response of a Λ system, *Phys. Rev. A* **57**, 4014 (1998).
- [13] S. E. Harris, Lasers without inversion: Interference of lifetime-broadened resonances, *Phys. Rev. Lett.* **62**, 1033 (1989).
- [14] M. O. Scully, S.-Y. Zhu, and A. Gavrielides, Degenerate quantum-beat laser: Lasing without inversion and inversion without lasing, *Phys. Rev. Lett.* **62**, 2813 (1989).
- [15] E. Paspalakis, S. Gong, and P. L. Knight, Spontaneous emission-induced coherent effects in absorption and dispersion of a V-type three-level atom, *Opt. Commun.* **152**, 293 (1998).
- [16] C.-L. Wang, A.-J. Li, X.-Y. Zhou, Z.-H. Kang, J. Yun, and J.-Y. Gao, Investigation of spontaneously generated coherence in dressed states of ^{85}Rb atoms, *Opt. Lett.* **33**, 687 (2008).
- [17] H. Ma, S. Gong, C. Liu, Z. Sun, and Z. Xu, Effects of spontaneous emission-induced coherence on population inversion in a ladder-type atomic system, *Opt. Commun.* **223**, 97 (2003).
- [18] D. G. Norris, L. A. Orozco, P. Barberis-Blostein, and H. J. Carmichael, Observation of ground-state quantum beats in atomic spontaneous emission, *Phys. Rev. Lett.* **105**, 123602 (2010).
- [19] C. Wang, Z. Kang, S. Tian, Y. Jiang, and J. Gao, Effect of spontaneously generated coherence on absorption in a V-type system: Investigation in dressed states, *Phys. Rev. A* **79**, 043810 (2009).
- [20] Y. Lien, G. Barontini, M. Scheucher, M. Mergenthaler, J. Goldwin, and E. A. Hinds, Observing coherence effects in an overdamped quantum system, *Nat. Commun.* **7**, 13933 (2016).
- [21] M. Bamba, A. Imamoğlu, I. Carusotto, and C. Ciuti, Origin of strong photon antibunching in weakly nonlinear photonic molecules, *Phys. Rev. A* **83**, 021802(R) (2011).
- [22] H. Flayac and V. Savona, Input-output theory of the unconventional photon blockade, *Phys. Rev. A* **88**, 033836 (2013).
- [23] A. Imamoğlu, H. Schmidt, G. Woods, and M. Deutsch, Strongly interacting photons in a nonlinear cavity, *Phys. Rev. Lett.* **79**, 1467 (1997).
- [24] R. Huang, A. Miranowicz, J.-Q. Liao, F. Nori, and H. Jing, Nonreciprocal photon blockade, *Phys. Rev. Lett.* **121**, 153601 (2018).
- [25] B. Lounis and M. Orrit, Single-photon sources, *Rep. Prog. Phys.* **68**, 1129 (2005).
- [26] S. Buckley, K. Rivoire, and J. Vučković, Engineered quantum dot single-photon sources, *Rep. Prog. Phys.* **75**, 126503 (2012).
- [27] G.-C. Shan, Z.-Q. Yin, C. H. Shek, and W. Huang, Single photon sources with single semiconductor quantum dots, *Front. Phys.* **9**, 170 (2014).
- [28] H. J. Kimble, M. Dagenais, and L. Mandel, Photon antibunching in resonance fluorescence, *Phys. Rev. Lett.* **39**, 691 (1977).
- [29] T. C. H. Liew and V. Savona, Single photons from coupled quantum modes, *Phys. Rev. Lett.* **104**, 183601 (2010).
- [30] H. Flayac and V. Savona, Unconventional photon blockade, *Phys. Rev. A* **96**, 053810 (2017).
- [31] H. J. Sniijders, J. A. Frey, J. Norman, H. Flayac, V. Savona, A. C. Gossard, J. E. Bowers, M. P. van Exter, D. Bouwmeester, and W. Löffler, Observation of the unconventional photon blockade, *Phys. Rev. Lett.* **121**, 043601 (2018).
- [32] W. Zhang, Z. Yu, Y. Liu, and Y. Peng, Optimal photon antibunching in a quantum-dot-bimodal-cavity system, *Phys. Rev. A* **89**, 043832 (2014).
- [33] K. Wu, W.-X. Zhong, G.-L. Cheng, and A.-X. Chen, Phase-controlled multimagnon blockade and magnon-induced tunneling in a hybrid superconducting system, *Phys. Rev. A* **103**, 052411 (2021).
- [34] C. Vaneph, A. Morvan, G. Aiello, M. Féchant, M. Aprili, J. Gabelli, and J. Estève, Observation of the unconventional photon blockade in the microwave domain, *Phys. Rev. Lett.* **121**, 043602 (2018).
- [35] J. Li, C. Ding, and Y. Wu, Enhanced photon antibunching via interference effects in a Δ configuration, *Phys. Rev. A* **100**, 033814 (2019).
- [36] R. Yalla, M. Sadgrove, K. P. Nayak, and K. Hakuta, Cavity quantum electrodynamics on a nanofiber using a composite photonic crystal cavity, *Phys. Rev. Lett.* **113**, 143601 (2014).
- [37] S. Kato and T. Aoki, Strong coupling between a trapped single atom and an all-fiber cavity, *Phys. Rev. Lett.* **115**, 093603 (2015).

- [38] K. P. Nayak, M. Sadgrove, R. Yalla, F. Le Kien, and K. Hakuta, Nanofiber quantum photonics, *J. Opt. (Bristol, U. K.)* **20**, 073001 (2018).
- [39] K. P. Nayak, J. Wang, and J. Keloth, Real-time observation of single atoms trapped and interfaced to a nanofiber cavity, *Phys. Rev. Lett.* **123**, 213602 (2019).
- [40] A. Kiraz, M. Atatüre, and A. Imamoglu, Quantum-dot single-photon sources: Prospects for applications in linear optics quantum-information processing, *Phys. Rev. A* **69**, 032305 (2004).
- [41] K. Stannigel, P. Komar, S. J. M. Habraken, S. D. Bennett, M. D. Lukin, P. Zoller, and P. Rabl, Optomechanical quantum information processing with photons and phonons, *Phys. Rev. Lett.* **109**, 013603 (2012).
- [42] A. Kuhn, M. Hennrich, and G. Rempe, Deterministic single-photon source for distributed quantum networking, *Phys. Rev. Lett.* **89**, 067901 (2002).
- [43] L. Aolita and S. P. Walborn, Quantum communication without alignment using multiple-qubit single-photon states, *Phys. Rev. Lett.* **98**, 100501 (2007).
- [44] Z. Wu, J. Li, and Y. Wu, Vacuum-induced quantum-beat-enabled photon antibunching, *Phys. Rev. A* **108**, 023727 (2023).
- [45] G. C. Hegerfeldt and M. B. Plenio, Quantum beats revisited: A quantum jump approach, *Quantum Opt.* **6**, 15 (1994).
- [46] K. Qu and G. S. Agarwal, Generating quadrature squeezed light with dissipative optomechanical coupling, *Phys. Rev. A* **91**, 063815 (2015).
- [47] J. Li, Y. Qu, R. Yu, and Y. Wu, Generation and control of optical frequency combs using cavity electromagnetically induced transparency, *Phys. Rev. A* **97**, 023826 (2018).
- [48] M. O. Scully and M. S. Zubairy, *Quantum Optics* (Cambridge University Press, Cambridge, UK, 1997).
- [49] P. Meystre and M. Sargent, *Elements of Quantum Optics* (Springer, Berlin, 2013).
- [50] H. J. Carmichael, *Statistical Methods in Quantum Optics 1: Master Equations and Fokker-Planck Equations* (Springer, New York, 1999).
- [51] G. S. Agarwal, *Quantum Optics* (Cambridge University Press, Cambridge, UK, 2013).
- [52] C. Navarrete-Benlloch, Introduction to quantum optics, [arXiv:2203.13206](https://arxiv.org/abs/2203.13206).
- [53] E. M. Purcell, Spontaneous emission probabilities at radio frequencies, *Phys. Rev.* **69**, 681 (1946).
- [54] R. Loudon, *The Quantum Theory of Light* (Oxford University, Oxford, UK, 2003).
- [55] A. Rundquist, M. Bajcsy, A. Majumdar, T. Sarmiento, K. Fischer, K. G. Lagoudakis, S. Buckley, A. Y. Piggott, and J. Vučković, Nonclassical higher-order photon correlations with a quantum dot strongly coupled to a photonic-crystal nanocavity, *Phys. Rev. A* **90**, 023846 (2014).
- [56] K. M. Birnbaum, A. Boca, R. Miller, A. D. Boozer, T. E. Northup, and H. J. Kimble, Photon blockade in an optical cavity with one trapped atom, *Nature (London)* **436**, 87 (2005).
- [57] E. Z. Casalengua, J. C. L. Carreño, F. P. Laussy, and E. del Valle, Conventional and unconventional photon statistics, *Laser Photonics Rev.* **14**, 1900279 (2020).
- [58] L.-J. Feng and S.-Q. Gong, Two-photon blockade generated and enhanced by mechanical squeezing, *Phys. Rev. A* **103**, 043509 (2021).
- [59] D. A. Steck, Rubidium 85 D line data, available online at <http://steck.us/alkalidata> (revision 2.2.3, 9 July 2021).
- [60] M. Hennrich, A. Kuhn, and G. Rempe, Transition from antibunching to bunching in cavity QED, *Phys. Rev. Lett.* **94**, 053604 (2005).
- [61] K. P. Nayak and K. Hakuta, Photonic crystal formation on optical nanofibers using femtosecond laser ablation technique, *Opt. Express* **21**, 2480 (2013).
- [62] J. Keloth, K. P. Nayak, and K. Hakuta, Fabrication of a centimeter-long cavity on a nanofiber for cavity quantum electrodynamics, *Opt. Lett.* **42**, 1003 (2017).
- [63] K. P. Nayak, F. Le Kien, Y. Kawai, K. Hakuta, K. Nakajima, H. T. Miyazaki, and Y. Sugimoto, Cavity formation on an optical nanofiber using focused ion beam milling technique, *Opt. Express* **19**, 14040 (2011).
- [64] F. Le Kien, K. P. Nayak, and K. Hakuta, Nanofibers with Bragg gratings from equidistant holes, *J. Mod. Opt.* **59**, 274 (2012).
- [65] W. Li, J. Du, V. G. Truong, and S. N. Chormaic, Optical nanofiber-based cavity induced by periodic air-nanohole arrays, *Appl. Phys. Lett.* **110**, 253102 (2017).
- [66] E. Vetsch, D. Reitz, G. Sagué, R. Schmidt, S. T. Dawkins, and A. Rauschenbeutel, Optical interface created by laser-cooled atoms trapped in the evanescent field surrounding an optical nanofiber, *Phys. Rev. Lett.* **104**, 203603 (2010).
- [67] A. Goban, K. S. Choi, D. J. Alton, D. Ding, C. Lacroûte, M. Pototschnig, T. Thiele, N. P. Stern, and H. J. Kimble, Demonstration of a state-insensitive, compensated nanofiber trap, *Phys. Rev. Lett.* **109**, 033603 (2012).
- [68] H. L. Sørensen, J.-B. Béguin, K. W. Kluge, I. Iakoupov, A. S. Sørensen, J. H. Müller, E. S. Polzik, and J. Appel, Coherent backscattering of light off one-dimensional atomic strings, *Phys. Rev. Lett.* **117**, 133604 (2016).
- [69] A. Goban, C.-L. Hung, J. D. Hood, S.-P. Yu, J. A. Muniz, O. Painter, and H. J. Kimble, Superradiance for atoms trapped along a photonic crystal waveguide, *Phys. Rev. Lett.* **115**, 063601 (2015).
- [70] Y. Meng, C. Liedl, S. Pucher, A. Rauschenbeutel, and P. Schneeweiss, Imaging and localizing individual atoms interfaced with a nanophotonic waveguide, *Phys. Rev. Lett.* **125**, 053603 (2020).
- [71] T. G. Tiecke, J. D. Thompson, N. P. de Leon, L. R. Liu, V. Vuletić, and M. D. Lukin, Nanophotonic quantum phase switch with a single atom, *Nature (London)* **508**, 241 (2014).
- [72] P. Samutpraphoot, T. Dordevic, P. L. Ocola, H. Bernien, C. Senko, V. Vuletić, and M. D. Lukin, Strong coupling of two individually controlled atoms via a nanophotonic cavity, *Phys. Rev. Lett.* **124**, 063602 (2020).
- [73] F. Le Kien and K. Hakuta, Cavity-enhanced channeling of emission from an atom into a nanofiber, *Phys. Rev. A* **80**, 053826 (2009).
- [74] F. Le Kien and K. Hakuta, Triggered generation of single guided photons from a single atom in a nanofiber cavity, *Phys. Rev. A* **83**, 043801 (2011).
- [75] C. Wuttke, M. Becker, S. Brückner, M. Rothhardt, and A. Rauschenbeutel, Nanofiber Fabry-Perot microresonator for nonlinear optics and cavity quantum electrodynamics, *Opt. Lett.* **37**, 1949 (2012).
- [76] B. B. Zhou, A. Baksic, H. Ribeiro, C. G. Yale, F. J. Heremans, P. C. Jerger, A. Auer, G. Burkard, A. A. Clerk, and D. D. Awschalom, Accelerated quantum control using superadiabatic

- dynamics in a solid-state lambda system, *Nat. Phys.* **13**, 330 (2017).
- [77] R. Li, S. Li, D. Yu, J. Qian, and W. Zhang, Optimal model for fewer-qubit cnot gates with Rydberg atoms, *Phys. Rev. Appl.* **17**, 024014 (2022).
- [78] J. Zhao, L. Wu, T. Li, Y.-x. Liu, F. Nori, Y. Liu, and J. Du, Phase-controlled pathway interferences and switchable fast-slow light in a cavity-magnon polariton system, *Phys. Rev. Appl.* **15**, 024056 (2021).
- [79] J. C. Loredo, M. A. Broome, P. Hilaire, O. Gazzano, I. Sagnes, A. Lemaître, M. P. Almeida, P. Senellart, and A. G. White, Boson sampling with single-photon Fock states from a bright solid-state source, *Phys. Rev. Lett.* **118**, 130503 (2017).
- [80] S. E. Thomas, M. Billard, N. Coste, S. C. Wein, Priya, H. Ollivier, O. Krebs, L. Tazaïrt, A. Harouri, A. Lemaître, I. Sagnes, C. Anton, L. Lanco, N. Somaschi, J. C. Loredo, and P. Senellart, Bright polarized single-photon source based on a linear dipole, *Phys. Rev. Lett.* **126**, 233601 (2021).
- [81] F. Zou, X.-Y. Zhang, X.-W. Xu, J.-F. Huang, and J.-Q. Liao, Multiphoton blockade in the two-photon Jaynes-Cummings model, *Phys. Rev. A* **102**, 053710 (2020).
- [82] D.-Y. Wang, C.-H. Bai, X. Han, S. Liu, S. Zhang, and H.-F. Wang, Enhanced photon blockade in an optomechanical system with parametric amplification, *Opt. Lett.* **45**, 2604 (2020).
- [83] X.-Y. Yao, H. Ali, F.-L. Li, and P.-B. Li, Nonreciprocal phonon blockade in a spinning acoustic ring cavity coupled to a two-level system, *Phys. Rev. Appl.* **17**, 054004 (2022).
- [84] D. Walls and G. Milburn, *Quantum Optics* (Springer, Berlin, 1994).
- [85] C. W. Gardiner and P. Zoller, *Quantum Noise* (Springer-Verlag, New York, 2005).
- [86] P. Senellart, G. Solomon, and A. White, High-performance semiconductor quantum-dot single-photon sources, *Nat. Nanotechnol.* **12**, 1026 (2017).
- [87] P. Kok, W. J. Munro, K. Nemoto, T. C. Ralph, J. P. Dowling, and G. J. Milburn, Linear optical quantum computing with photonic qubits, *Rev. Mod. Phys.* **79**, 135 (2007).
- [88] D. Press, S. Götzinger, S. Reitzenstein, C. Hofmann, A. Löffler, M. Kamp, A. Forchel, and Y. Yamamoto, Photon antibunching from a single quantum-dot-microcavity system in the strong coupling regime, *Phys. Rev. Lett.* **98**, 117402 (2007).
- [89] X. Cao, M. Zopf, and F. Ding, Telecom wavelength single photon sources, *J. Semicond.* **40**, 071901 (2019).
- [90] J. Yang, C. Nawrath, R. Keil, R. Joos, X. Zhang, B. Höfer, Y. Chen, M. Zopf, M. Jetter, S. L. Portalupi, F. Ding, P. Michler, and O. G. Schmidt, Quantum dot-based broadband optical antenna for efficient extraction of single photons in the telecom O-band, *Opt. Express* **28**, 19457 (2020).
- [91] C. Couteau, S. Barz, T. Durt, T. Gerrits, J. Huwer, R. Prevedel, J. Rarity, A. Shields, and G. Weihs, Applications of single photons to quantum communication and computing, *Nat. Rev. Phys.* **5**, 326 (2023).
- [92] C. Couteau, S. Barz, T. Durt, T. Gerrits, J. Huwer, R. Prevedel, J. Rarity, A. Shields, and G. Weihs, Applications of single photons in quantum metrology, biology and the foundations of quantum physics, *Nat. Rev. Phys.* **5**, 354 (2023).
- [93] H. J. Carmichael, *Statistical Methods in Quantum Optics 2: Nonclassical Fields* (Springer, Berlin, 2008).
- [94] R. Sáez-Blázquez, J. Feist, F. J. García-Vidal, and A. I. Fernández-Domínguez, Photon statistics in collective strong coupling: Nanocavities and microcavities, *Phys. Rev. A* **98**, 013839 (2018).
- [95] F. Minganti, A. Miranowicz, R. W. Chhajlany, and F. Nori, Quantum exceptional points of non-Hermitian Hamiltonians and Liouvillians: The effects of quantum jumps, *Phys. Rev. A* **100**, 062131 (2019).
- [96] B. Rousseaux, D. G. Baranov, T. J. Antosiewicz, T. Shegai, and G. Johansson, Strong coupling as an interplay of quantum emitter hybridization with plasmonic dark and bright modes, *Phys. Rev. Res.* **2**, 033056 (2020).
- [97] Y. H. Zhou, H. Z. Shen, and X. X. Yi, Unconventional photon blockade with second-order nonlinearity, *Phys. Rev. A* **92**, 023838 (2015).
- [98] Y. Liu, G. Wang, Y. Liu, and F. Nori, Mode coupling and photon antibunching in a bimodal cavity containing a dipole quantum emitter, *Phys. Rev. A* **93**, 013856 (2016).